Annu. Rev. Phys. Chem. 1998. 49:569–638

INTERFACES AND THIN FILMS AS SEEN BY BOUND ELECTROMAGNETIC WAVES

Wolfgang Knoll
Max-Planck-Institut für Polymerforschung, Ackermannweg 10, 55128 Mainz, Germany; Department of Chemical Engineering, Center on Polymer Interfaces and Macromolecular Assemblies, Stanford University, Stanford, CA 94305-5025; Frontier Research Program, The Institute of Physical and Chemical Research (RIKEN), Wako, Saitama, Japan; e-mail: knoll@mpip-mainz.mpg.de

KEY WORDS: evanescent wave optics, plasmon surface polaritons, guided optical waves, interfacial architectures, ultrathin organic films

ABSTRACT

This contribution summarizes the use of plasmon surface polaritons and guided optical waves for the characterization of interfaces and thin organic films. After a short introduction to the theoretical background of evanescent wave optics, examples are given that show how this interfacial "light" can be employed to monitor thin coatings at a solid/air or solid/liquid interface. Examples are given for a very sensitive thickness determination of samples ranging from self-assembled monolayers, to multilayer assemblies prepared by the Langmuir/Blodgett/Kuhn technique or by the alternate polyelectrolyte deposition. These are complemented by the demonstration of the potential of the technique to also monitor time-dependent processes in a kinetic mode. Here, we put an emphasis on the combination set-up of surface plasmon optics with electrochemical techniques, allowing for the on-line characterization of various surface functionalization strategies, e.g. for (bio-) sensor purposes.

INTRODUCTION

The term evanescent wave optics summarizes a number of optical phenomena and techniques associated with the total internal reflection of light at the boundary between two media of different optical properties described by their

0066-426X/98/1001-0569$08.00

different dielectric functions, ε_i (1). This can be observed e.g. at the boundary between a glass prism and water as it is sketched in Figure 1(*a*): A plane wave, e.g. from a laser light source (wavelength λ) impinging upon that interface from the glass side, i.e. from the side of the material with the higher refractive index, $n_p = \sqrt{\varepsilon_p}$, will be totally (internally) reflected if the angle of incidence exceeds a critical value θ_c. This can be easily observed by recording the reflected intensity, e.g. with a diode detector, as a function of the angle of incidence, θ. Figure 1(*b*) shows a typical experiment: At incident angles smaller than θ_c, most of the incoming light is transmitted and hence the reflected intensity is low. As one approaches θ_c, however, the reflectivity R (the ratio between reflected and incoming intensity) reaches unity. θ_c is given by Snell's law and depends on the refractive indices of the two media. In the case of a glass/water interface, one obtains $\sin\theta_c = \frac{n_d}{n_p}$ with $n_d = \sqrt{\varepsilon_d}$ being the refractive index of the water.

If one inspects the details of the optical field near the interface, e.g. experimentally by a scanning near-field optical microscope (SNOM) or theoretically by treating the problem within Maxwell's theory, one finds that above θ_c the optical E-field along the propagation direction, E_x, has the usual oscillatory character of an electromagnetic mode. The component perpendicular to the interface, E_z, however, does not fall to zero abruptly, but decays exponentially with a decay length l which is a function of the angle of incidence

$$l = \frac{\lambda}{2\pi\sqrt{(n \cdot \sin\theta)^2 - 1}}, \quad \theta > \theta_c. \qquad 1.$$

Such an electromagnetic field distribution is called an evanescent wave.

In addition to the advantage that only the near-interface range is "illuminated" by this wave, resulting in a surface selectivity when using this surface-bound light for optical experiments, its intensity, I_s, is slightly enhanced compared to the incoming plane wave [by a factor of 4 at θ_c, see Figure 1(*c*)] which results in a modest sensitivity enhancement for optical experiments. A whole family of spectroscopies, the most prominent one being total internal reflection fluorescence (TIRF) spectroscopy (2), has emerged from this configuration.

Furthermore, other formats monitor the different reflection behavior for different polarizations, giving rise to interesting phenomena and analytical power in evanescent ellipsometry configurations, in particular when dealing with optically anisotropic media next to a coupling prism (3, 4).

This review discusses several extensions of this basic principle. The first one is concerned with the excitation of plasmon surface polaritons (PSP) at the interface between a noble metal and a dielectric medium (5). We show that

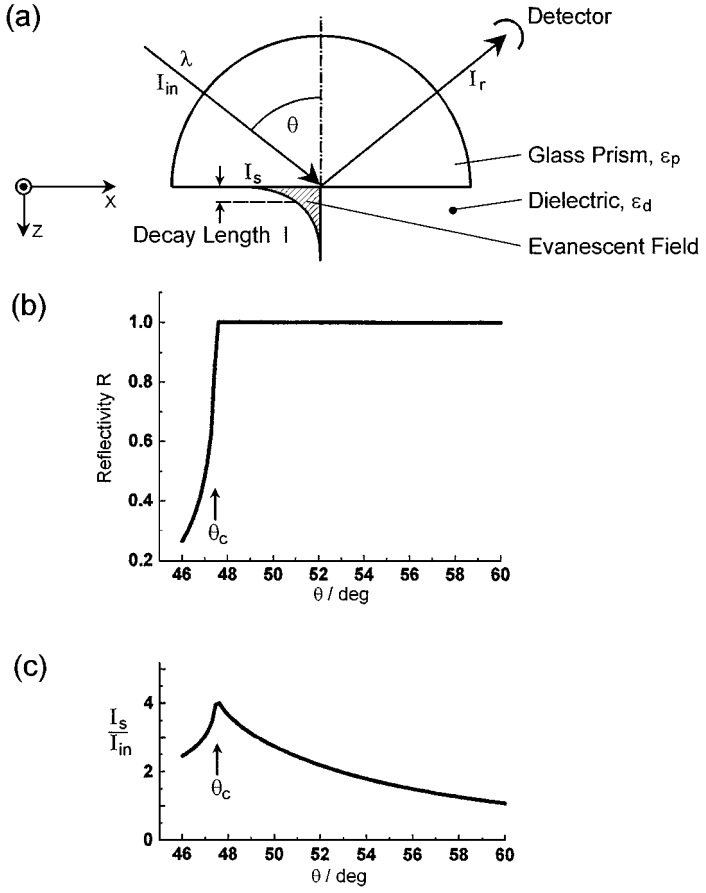

Figure 1 (*a*) Total internal reflection of a plane wave of wavelength λ and intensity I_{in} at the base of a glass prism with ε_p in contact with a dielectric medium of $\varepsilon_d < \varepsilon_p$. The reflected light is monitored with a detector. For incident angles $\theta > \theta_c$, the critical angle for total internal reflection, the evanescent field at the interface decays exponentially into the dielectric with a decay length l. (*b*) Reflectivity, i.e. I_r/I_{in}, as a function of the incident angle θ. θ_c denotes the critical angle for total internal reflection, and is given by $\sin\theta_c = \sqrt{\frac{\varepsilon_d}{\varepsilon_p}}$. The curve was calculated with $\varepsilon_p = 3.4036$, $\varepsilon_d = 1.778$. (*c*) Intensity enhancement, I_s/I_{in}, at the interface ($z = 0$) as a function of the incident angle θ.

the (nearly) free electron gas in the metal acts as a resonator driven by the incoming photon field, giving rise to substantial intensity enhancements (6, 7) compared to the mere dielectric configuration of Figure 1. We demonstrate that, again, we are dealing with an evanescent, i.e. bound, electromagnetic mode propagating along the metal/dielectric interface and give a number of examples of how this surface light can be employed to monitor interfacial properties and processes sensitively, or to characterize the optical properties of ultrathin coatings deposited onto the interface (8).

The second extension concerns guided optical waves (GOW) (9). We show that once a minimum thickness of a coating layer (deposited on top of a solid support) is reached, new film resonances can be observed as narrow dips in the angular reflectivity scans (8). These additional resonances originate from guided optical modes excited in the thin film, the optical thickness of which fulfills the well-known eigenvalue equation for optical waveguide modes. These modes propagate again as electromagnetic waves bound to the thin film waveguide structure with an evanescent tail reaching out into the surrounding medium (see Figure 8). Again, this evanescent surface light can be used to monitor very sensitively surface reactions and processes. As far as thin film studies are concerned, however, the real advantage of optical waveguide spectroscopy (OWS) originates from the fact that modes of both polarizations, i.e. transversal magnetic (TM- or p-polarized) and transversal electric (TE- or s-polarized) modes, can be excited by probing different components of the indicatrix (the index ellipsoid) of the thin film material (10). This is particularly important and helpful for the characterization of optically anisotropic layers used in integrated optics configurations.

This review is organized in the following way: In the next section we give a brief summary of the Maxwell treatment of the optical configuration, thus providing a short introduction to the theoretical background needed to describe surface plasmons and guided optical waves in various formats. In particular, we demonstrate the need for coupling devices, i.e. prisms and gratings, for the excitation of these modes by laser light. In the subsequent section we give (*a*) a broad spectrum of experimental configurations based on the attenuated total internal reflection (ATR) mode of operation, and (*b*) we show the usefulness of surface plasmon and waveguide spectroscopy for the characterization of the structural and optical properties of the layer architectures for a variety of thin film samples. Then we turn to the use of gratings as coupling devices and demonstrate, in particular, a novel mode of operation based on the noncollinear coupling of wavevectors. As a special format of channel waveguides, we present an integrated Mach-Zehnder interferometer and its application as a sensor for biorecognition reactions.

BOUND ELECTROMAGNETIC MODES

Plasmon Surface Polaritons at a Noble Metal/Dielectric Interface

We consider an interface in the xy-plane between two half-infinite spaces, 1 and 2, of materials the optical properties of which are described by their complex frequency-dependent dielectric functions $\tilde{\varepsilon}_1(\omega)$ and $\tilde{\varepsilon}_2(\omega)$, respectively. We ignore magnetic materials. Surface polaritons can only be excited at such an interface if the dielectric displacement $\vec{D}$ of the electromagnetic mode has a component normal to the surface ($\|\vec{z}$) which can induce a surface charge density σ,

$$(\vec{D}_2 - \vec{D}_1) \cdot \vec{z} = 4\pi\sigma. \qquad 2.$$

S-polarized light propagating along the x-direction possesses only electric field components, $\vec{E}_i$, parallel to the surface ($\|$y-direction), i.e. transversal electric (TE) waves have $\vec{E}_i = (0, E_y, 0)$, and hence are unable to excite surface polaritons. Only p-polarized light (transversal magnetic TM) modes with $E = (E_x, 0, E_z)$, or, equivalently, $\vec{H} = (0, H_y, 0)$, can couple to such modes. The resulting surface electromagnetic wave, therefore, will have the following general form

$$\vec{A}_1 = \vec{A}_{10} e^{i(\vec{k}_{x1}\vec{x} + \vec{k}_{z1}\vec{z} - \omega t)} \text{ in medium 1, } z < 0 \qquad 3a.$$

and

$$\vec{A}_2 = \vec{A}_{20} e^{i(\vec{k}_{x2}\vec{x} - \vec{k}_{z2}\vec{z} - \omega t)} \text{ in medium 2, } z > 0, \qquad 3b.$$

where $\vec{A}$ stands for $\vec{E}$ and $\vec{H}$; $\vec{k}_{x1}$, and $\vec{k}_{x2}$ are the wavevectors in the x-direction; $\vec{k}_{z1}$, and $\vec{k}_{z2}$ those in the z-direction, i.e. normal to the interface; and ω is the angular frequency. Both fields $\vec{E}$ and $\vec{H}$ must fulfill the Maxwell equations:

$$\nabla \cdot \vec{H} = 0, \qquad 4.$$

$$\nabla \cdot \vec{E} = 0, \qquad 5.$$

$$\nabla \times \vec{E} + \frac{1}{c}\frac{\partial \vec{H}}{\partial t} = 0, \qquad 6.$$

$$\nabla \times \vec{H} - \frac{\varepsilon}{c}\frac{\partial \vec{E}}{\partial t} = 0, \qquad 7.$$

with c being the speed of light in vacuo and ε the dielectric function of the material. The tangential components of $\vec{E}$ and $\vec{H}$ have to be equal at the interface, i.e.

$$E_{x1} = E_{x2} \tag{8.}$$

and

$$H_{y1} = H_{y2}. \tag{9.}$$

From Equation 8 it follows immediately that $k_{x1} = k_{x2} = k_x$. On the other hand, it follows from Equations 3 and 7 that

$$k_{z1} H_{y1} = \frac{\omega}{c} \varepsilon_1 E_{x1} \tag{10.}$$

and

$$k_{z2} H_{y2} = -\frac{\omega}{c} \varepsilon_2 E_{x2}. \tag{11.}$$

This leads to the only nontrivial solution if:

$$\frac{k_{z1}}{k_{z2}} = -\frac{\varepsilon_1}{\varepsilon_2}. \tag{12.}$$

Equation 12 indicates that surface electromagnetic modes can only be excited at interfaces between two media with dielectric constants of opposite sign. For a material in contact with a dielectric medium the dielectric constant, ε_d, of which is positive, this can be fulfilled for a whole variety of possible elementary excitations provided their oscillator strength is sufficiently strong to result—for a narrow spectral range—in a negative ε. Within certain limits, this can be the case for phonons as well as for excitons. The coupling of these excitations to an electromagnetic field has been shown to produce phonon surface polariton or exciton surface polariton modes, respectively.

Here we are dealing with the interface between a metal with its complex dielectric function ($\tilde{\varepsilon}_m = \varepsilon'_m + i\varepsilon''_m$) and a dielectric material ($\tilde{\varepsilon}_d = \varepsilon'_d + i\varepsilon''_d$), hence, with coupling the collective plasma oscillations of the nearly free electron gas in a metal to an electromagnetic field (5). These excitations are called plasmon surface polaritons (PSP) or surface plasmons, for short. From Equations 6, 7, 10, and 11 we obtain

$$k_x^2 + k_{zd}^2 = \left(\frac{\omega}{c}\right)^2 \varepsilon_d \tag{13.}$$

or

$$k_{zd} = \sqrt{\varepsilon_d \left(\frac{\omega}{c}\right)^2 - k_x^2}. \tag{14.}$$

With Equation 12 this leads to the dispersion relationships (i.e. the energy-momentum relation) for surface plasmons at a metal/dielectric interface:

$$k_x = \frac{\omega}{c}\sqrt{\frac{\varepsilon_m \cdot \varepsilon_d}{(\varepsilon_m + \varepsilon_d)}}. \qquad 15.$$

A few details are noteworthy: 1. In the usual treatment, ω is taken to be real. Since $\tilde{\varepsilon}_m$ is complex, $\tilde{k}_x$ is also complex, i.e. $\tilde{k}_x = k'_x + ik''_x$. As a consequence, PSP modes propagating along a metal/dielectric interface exhibit a finite propagation length, L_x, given by $L_x = \frac{1}{k''_x}$. This decay has a strong impact on lateral resolution that we want to obtain in the characterization of laterally structured samples investigated with plasmon or waveguide light in a microscopic setup (11). 2. In the frequency (spectral) range of interest we have:

$$\sqrt{\frac{\varepsilon_m \cdot \varepsilon_d}{(\varepsilon_m + \varepsilon_d)}} \geq \sqrt{\varepsilon_d}. \qquad 16.$$

This has two important consequences. The first can be seen from Equation 14. Inserting Equation 16 shows that in this case the z-component of the PSP wave vector is purely imaginary. From Equation 3 we see that the surface plasmon is a bound, nonradiative evanescent wave with a field amplitude, the maximum of which is at the interface ($z = 0$) and which is decaying exponentially into the dielectric (and into the metal). The mode is propagating as a damped oscillatory wave (refer to Figure 2). All parameters characterizing the properties of PSPs can be quantitatively described on the basis of the dielectric functions of the

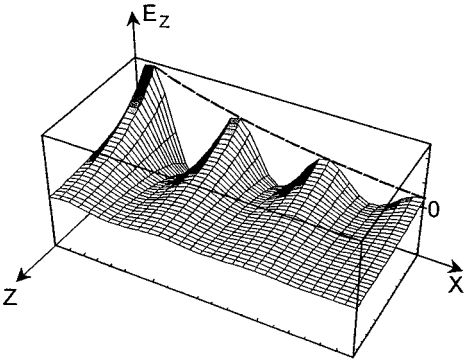

Figure 2 Schematic of the evanescent character of a surface plasmon mode excited at a metal/dielectric interface in the x-, y-plane propagating as a damped oscillatory wave in the x-direction. The electric field components along the z-direction, normal to the interface, decay exponentially, here shown for the E_z component.

involved materials, e.g. the exponential decay of the optical field intensity normal to an Ag/dielectric interface. The penetration depth, l_c, of this light into the dielectric medium is found to be a few hundred nanometers only, and again it is this surface specificity that makes it such an interesting probe field.

The second consequence of Equation 16 is that the momentum of a free photon propagating in a dielectric medium,

$$k_{ph} = \frac{\omega}{c} \cdot \sqrt{\varepsilon_d}, \qquad 17.$$

is always smaller than the momentum of a surface plasmon mode, k_{sp}, propagating along an interface between that same medium and the metal [see Figure 3(*a*)]. The dispersion of photons is described by the light line, $\omega = c_d \cdot k_{ph}$ [Figure 3(*b*)], with $c_d = c/\sqrt{\varepsilon_d}$.

For the excitation of surface plasmons, only the photon wave vector projection to the x-direction is the relevant parameter. For a simple reflection of photons (with energy $\hbar\omega_L$, e.g. from a laser) at a planar dielectric/metal interface, this means that by changing the angle of incidence, θ, one can tune $k_{ph}^x = k_{ph} \cdot \sin\theta$ from zero at normal incidence [point 0 in Figure 3(*b*)] to the full wave vector k_{ph} at grazing incidence [point *A* in Figure 3(*b*)]. Equation 15 or 16, however, tells us that this is not sufficient to fulfill—in addition to the energy conservation—the momentum-matching condition for resonant PSP excitation because, for very low energies, the PSP dispersion curve [Figure 3(*b*)] asymptotically reaches the light line, whereas for higher energies it approaches the cutoff angular frequency $\omega_{\max}$ determined by the plasma frequency of the employed metal, ω_p:

$$\omega_{\max} = \omega_p/\sqrt{1+\varepsilon_d}. \qquad 18.$$

One way to overcome this problem was introduced by the experimental setup called the Otto-configuration (12) shown schematically in Figure 4(*a*). Photons are not coupled directly to the metal/dielectric interface, but via the evanescent tail of light totally internally reflected at the base of a high-index prism (with $\varepsilon_p > \varepsilon_d$). This light is characterized by a larger momentum [Figure 3(*b*), *dash-dotted line*] that for a certain spectral range can exceed the momentum of the PSP to be excited at the metal surface. So, by choosing the appropriate angle of incidence θ_0 [point *B* in Figure 3(*b*)], resonant coupling between evanescent photons and surface plasmons can be obtained. The corresponding momentum-matching condition is schematically given in Figure 3(*c*).

Experimentally, this resonant coupling is observed by monitoring, as a function of the incident angle, the laser light of energy $\hbar\omega_L$ that is reflected by the base of the prism, which shows a sharp minimum [see also Figure 5(*a*)]. The major technical drawback of this configuration is the need to get the metal

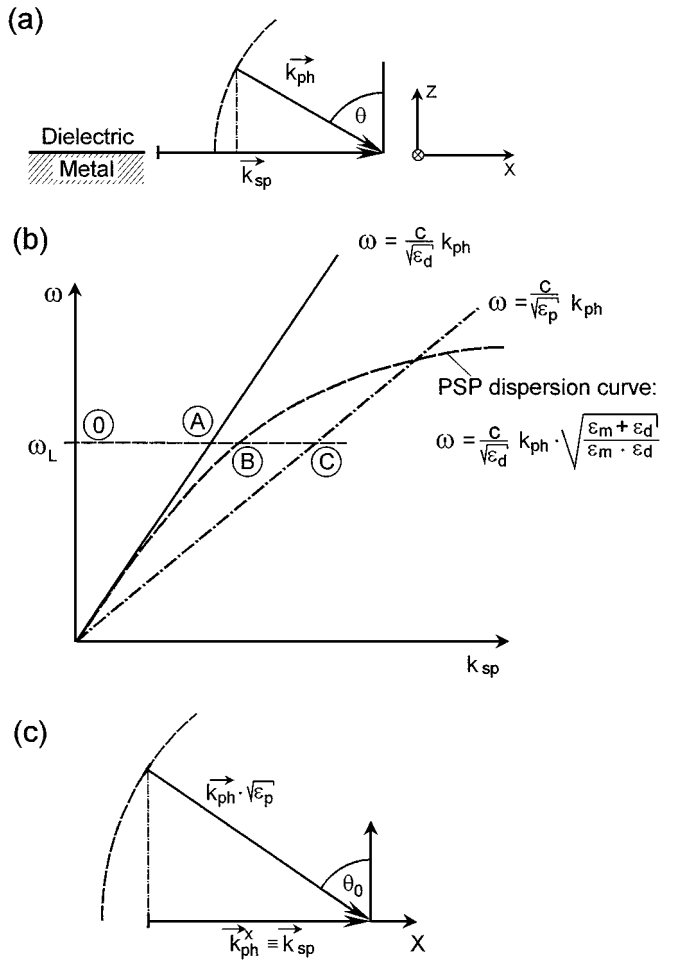

Figure 3 (*a*) Momentum relation between a surface plasmon, $\vec{k}_{sp}$, propagating along x and a photon, $\vec{k}_{ph}$, incident at the metal/dielectric interface at an angle θ. At any angles θ, $|\vec{k}_{ph}| < |\vec{k}_{sp}|$. (*b*) Dispersion relation of a photon traveling as a plane wave in the dielectric medium, $\omega = c_d k_{ph}$, with $c_d = \frac{c}{\sqrt{\varepsilon_d}}$ the speed of light in the dielectric (*full line*), and of a photon propagating in the prism, $\omega = c_p k_{ph}$, $c_p = \frac{c}{\sqrt{\varepsilon_p}}$, *dash-dotted line. Dashed curve*, dispersion of the surface plasmon mode propagating along the metal/dielectric interface. The meaning of 0, A, B, and C is given in the text. (*c*) Wavevector matching condition for the resonant coupling of photons traveling in the prism: At the incident angle θ_0, the photon projection along the x-coordinate, $\vec{k}_{ph}^{x}$, matches the PSP wavevector $\vec{k}_{sp}$. For details, see text.

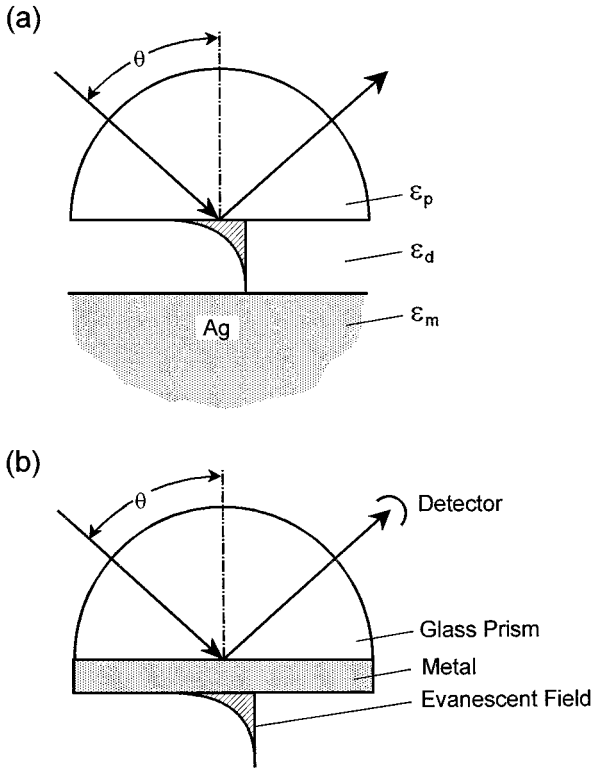

Figure 4 (*a*) The Otto configuration is based on the total internal reflection of a plane wave incident at an angle θ at the base of a prism. The evanescent tail of this inhomogeneous wave can excite PSP states at an Ag-dielectric interface, provided the coupling gap is sufficiently narrow. (*b*) Attenuated total internal reflection (ATR) construct for PSP excitation in the Kretschmann geometry. A thin metal film ($d \sim 50$ nm) is evaporated onto the base of the prism and acts as a resonator driven by the photon field incident at an angle θ.

surface close enough to the prism base, typically to within ∼200 nm. Even a few dust particles can act as spacers, thus preventing efficient coupling. So, despite its potential importance for the optical analysis of polymer-coated bulk metal samples, this version of surface plasmon spectroscopy has not gained any practical importance (13).

By far the most widespread version of surface plasmon spectroscopy is based on the experimental configuration introduced by Kretschmann and Raether (14) [Figure 4(*b*)]. Conceptually, this scheme for exciting PSPs is rather similar to the aforementioned technique, with the exception that this time the (high-momentum) photons in the prism couple through a very thin metal layer

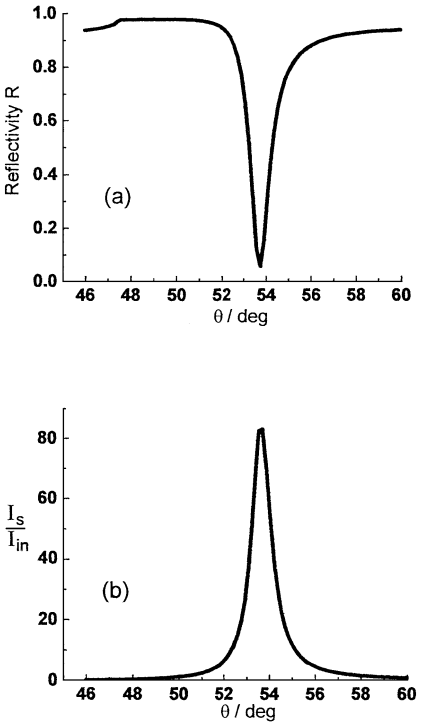

Figure 5 (*a*) Calculated reflectivity and (*b*) enhancement of the interfacial optical intensity, I_s / I_{in}, for a three-layer system: glass ($\varepsilon_p = 3.4036$)/Ag($\tilde{\varepsilon}_{Ag} = -17 + i \cdot 0.5, d = 50$ nm)/water ($\varepsilon_d = 1.778$).

(typically, approximately 45 to 50 nm thick, evaporated directly onto the base of the prism or onto a glass slide which is then index-matched to the base of the prism) to the PSP states at the other side in contact with the dielectric medium. Qualitatively, the same consideration for energy- and momentum-matching apply as discussed for Figure 4(*a*) [see also Figure 3(*b*)]; however, quantitatively one has to take into account that the finite thickness of the metal layer causes some modifications of the dispersion behavior of the PSP modes. In particular, the possibility of coupling out some of the surface plasmon light through the thin metal layer and the prism opens a new, radiative-loss channel for PSPs in addition to the intrinsic dissipation in the metal (6). One then can describe the angular dependence of the reflectivity by solving Maxwell's or Fresnel's equations for this layer architecture of glass/Ag-layer/dielectric. An example is given in Figure 5(*a*), based on the known parameters ε_p, ε_d, and the values for $\tilde{\varepsilon}_m = \varepsilon'_m + i\varepsilon''_m$, and d, the metal layer thickness.

One very important parameter, the angular dependence of the interfacial intensity at ($z = 0$) is displayed in Figure 5(b). One can see that assuming a perfect interface, i.e. describing the layer architecture that leads to the reflectivity curve of Figure 5(a), with perfectly flat interfaces exhibiting no roughness or other imperfections, enhancement factors of more than 80 for the surface plasmon light compared to the incoupling laser light can be obtained. In real experimental situations the enhancement might be more moderate, but still exists (7, 15). This intensity enhancement is the source of the sensitivity gain that was found in many spectroscopic experiments with surface plasmon light, in particular, demonstrated for Brillouin- and Raman-spectroscopies (16), but also for fluorescence optical experiments using PSP modes as the exciting field (17, 18).

At this point, one should emphasize the resonance character of the excitation of a surface plasmon mode: As for any oscillator, the maximum amplitude and the width of the resonance curve depend on the degree of damping that exists in the system. For the excitation of PSP, the dissipation of energy in the metal is the relevant damping mechanism described in the Maxwell treatment by the imaginary (loss) part of the dielectric function, ε_m''. For optical frequencies, Ag is the metal with the smallest ε_{Ag}'', followed by Au. Therefore, for a given laser wavelength λ, the PSP reflectivity curve for a Ag/air interface has the smallest width, $\Delta\theta \simeq 0.5$ deg @ $\lambda = 633$ nm, and consequently shows the highest enhancement factor for the intensity [refer to Figure 5(b)]. The resonance at an Au/air interface is $\Delta\theta \approx$ 2–3 deg wide [depending on the homogeneity of the evaporated Au layer whose granular structure with the many grain boundaries gives rise to additional (scattering) loss mechanisms], and the enhancement is "only" a factor of 20 (@ $\lambda = 633$ nm). Of course, the strong frequency dependence of $\tilde{\varepsilon}_m(\omega) = \varepsilon_m'(\omega) + \varepsilon_m''(\omega)$ gives rise to a strong wavelength dependence of the width and the enhancement factor.

A completely different coupling mechanism is given for a metal/dielectric interface that is periodically corrugated [see Figure 6(a)]: Such a metallic grating structure is used in (grating) spectrometers as the dispersive element, and it was such a grating that gave rise to the first observation of an optically excited PSP, known in the literature as Wood's anomaly (6).

Again, the relevant principle that governs the coupling between a laser photon and a surface plasmon is given by the momentum-matching condition. The corresponding scheme is shown in Figure 6(b). As in the case of the prism coupling, resonance is obtained if for a given energy $\hbar\omega_L$ of a laser photon the corresponding surface plasmon momentum on the dispersion curve can be matched. As highlighted in Figure 6(c), this can be achieved by the vectorial collinear addition of the projection of the photon wavevector to the x-axis, k_{ph}^x, and the grating wavevector $\vec{G}$, the magnitude of which is given by the grating constant $\Lambda : |\vec{G}| = 2\pi/\Lambda$. In the example schematically given in

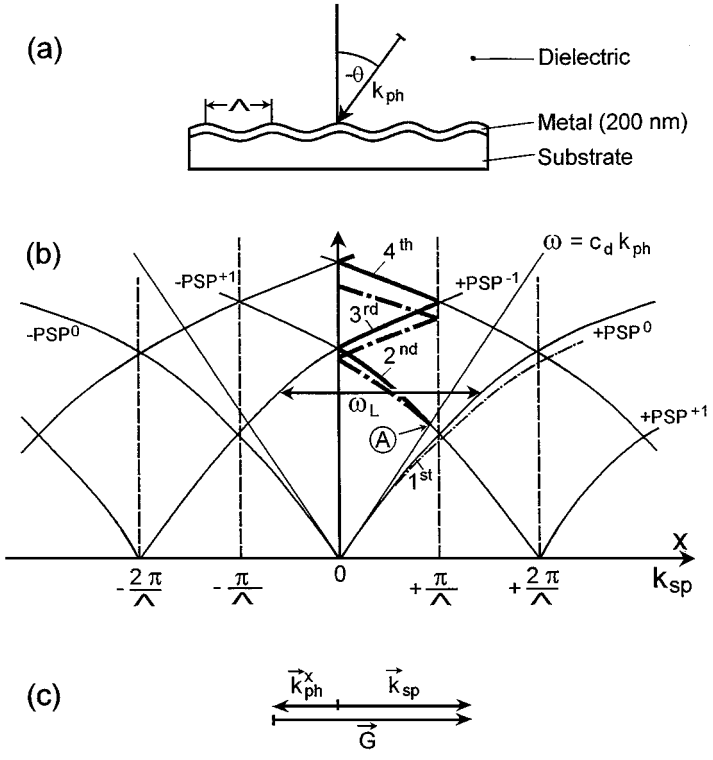

Figure 6 (*a*) Coupling scheme of a photon with wavevector k_{ph}, incident from the dielectric medium to a metal grating of grating constant Λ at an angle $-\theta$. The grating is prepared by evaporating a relatively thick layer ($d \sim 200$ nm) of Ag or Au onto a substrate with a corresponding surface corrugation. (*b*) Dispersion branches at a metal grating/dielectric interface. In addition to the two dispersion branches PSP^0 and $-\mathrm{PSP}^0$ originating at $k_{sp} = 0$, new branches appear, shifted by $\pm m \cdot \vec{G}$, with $|\vec{G}| = 2\pi/\Lambda$. In the reduced Brillouin zone scheme between $0 < k_{sp} < \pi/\Lambda$, a sequence of branches (*1st, 2nd, 3rd, 4th, etc.*) "zigzags" between the two boundaries with increasing energy. Coupling of photons to these PSP states is possible from point *A* on, at which the backwards-traveling PSP modes originating at $2\pi/\Lambda$ on the branch $-\mathrm{PSP}^{+1}$ cross the light line $\omega = c_d \cdot k_{ph}$. For higher laser energies $\hbar\omega_L$, the collinear wavevector addition of k_{ph}^x and a multiple of the grating vector $m \cdot \vec{G}$ matches the PSP wavevector k_{sp}. This is again given in (*c*) for $m = 1$. The *dash-dotted curve* in (*b*) gives the dispersion behavior for a grating coated with a thin layer of $\varepsilon_{layer} > \varepsilon_d$.

Figure 6, this means that for the negative angle of incidence $-\theta$, $\vec{k}_{ph}^{x}$ is pointing into the (−x)-direction. The addition of $+\vec{G}$ launches a surface plasmon mode propagating in the (+x)-direction at a wavevector $\vec{k}_{sp}$.

Another way to look at this experimental situation comes from the analogy to the description of phonons excited in the periodic lattice configuration of a single crystal: The translational symmetry of our grating structure leads to a Brillouin zone scheme with new dispersion branches originating at multiples of $|\vec{G}| = \pm 2\pi/\Lambda$, i.e.

$$\omega(\vec{k}_{sp}) = \omega(\vec{k}_{sp} \pm m\vec{G}). \qquad 19.$$

In the reduced Brillouin zone scheme, ranging from 0 to $+\pi/\Lambda$, new dispersion branches hence appear that look like they are being "back-folded" or reflected at $|\vec{k}_{sp}| = 0$ or $|\vec{k}_{sp}| = \pi/\Lambda$ [*bold zigzag curve* in Figure 6(*b*)]. The first section of this curve [in Figure 6(*b*)] corresponds to surface plasmons with an energy momentum relation that is inaccessible for photons: For any given energy $\hbar\omega_L$ the corresponding momentum of the photon is too small to match that of the surface plasmon mode—the dispersion of these PSPs still lies on the "right hand side" of the light line, $\omega = \frac{c}{\sqrt{\varepsilon_d}} k_{ph}$ (see Figure 3). Only for the second branch [in Figure 6(*b*)], from point *A* on, the dispersion curve of PSP lies "on the left side" of the light line and hence can be reached by the proper choice of the incident angle of the exciting laser beam [see Figure 6(*a*)].

What is important in the context of our interest in using this surface light for the characterization of interfaces and thin films is the question regarding how sensitively PSPs depend on the optical properties of the dielectric half-space. From Equation 15 we can see that for a given energy $\hbar\omega_L$ the momentum of surface plasmons increases with an increase of the dielectric constant ε_d of the surrounding medium. This means that exciting PSP at an Au/water interface requires a higher angle of incidence than for PSP of the same energy, but excited at a Au/air interface [refer to Figure 5(*a*) and Figure 7(*c*)]. In practice, this can imply that for the Kretschmann coupling scheme, a prism with a higher

Figure 7 (*a*) Dispersion relation, ω vs. k_{sp}, of plasmon surface polaritons at an Ag-air interface (PSP[a], *solid curve*) and at an Ag-dielectric coating-air interface (PSP[b], *broken curve*). Laser light of energy $\hbar\omega_L$ couples at angles θ_0 and θ_1, respectively, given by the energy and momentum matching condition (see the intersection of the *horizontal line* at ω_L with the two dispersion curves). (*b*) Schematic of the experimental system for surface plasmon spectroscopy. (*c*) Reflectivity curves obtained for a bare Au-film; *curve a*, evaporated onto a BK7-glass prism; *curve b*, after self-assembling a monomolecular layer of HS-$(CH_2)_{21}$-OH. The symbols are experimental data points; the full curves are Fresnel fits with $\varepsilon_{BK7} = 2.29$, $\tilde{\varepsilon}_{Au} = -12.45 + i \cdot 1.3$, $d_{Au} = 46.9$ nm, $\varepsilon_{layer} = 2.1025$, $d_{layer} = 2.65$ nm. Data were taken at $\lambda = 633$ nm in air.

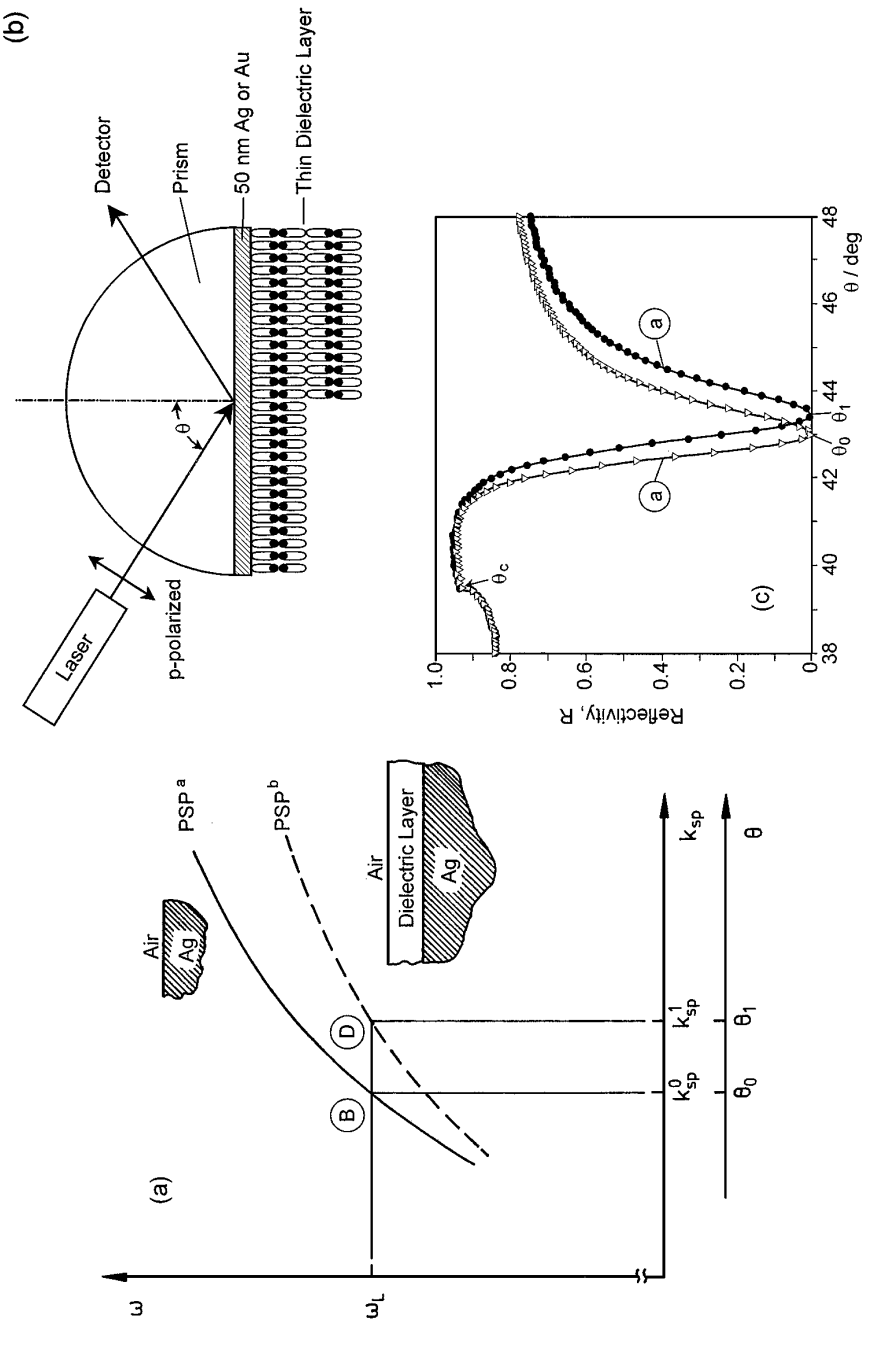
(a)
ω
ω_L
PSP a
PSP b
Air
Ag
B
D
Air
Dielectric Layer
Ag
k_{sp}
k^0_{sp}
k^1_{sp}
θ
θ_0
θ_1
(b)
Detector
Prism
50 nm Ag or Au
Thin Dielectric Layer
θ
Laser
p-polarized
(c)
Reflectivity, R
1.0
0.8
0.6
0.4
0.2
0
38
40
42
44
46
48
θ / deg
θ_c
a
a
θ_0
θ_1

refractive index is required for the excitation of PSP at a metal/liquid interface compared to measurements in air. The grating coupler is more versatile in this sense, and changing from one material to another simply requires the corresponding retuning of the incident angle θ.

In experiments aimed at characterizing thin films, however, we modify the optical properties of only a narrow slice of the dielectric half-space that is probed by the evanescent PSP field. For a qualitative picture only, we note that depositing an ultrathin layer (with a thickness of $d \ll 2\pi/k_{zd}$) of a material with an index of refraction $n_{layer} = \sqrt{\varepsilon_{layer}}$ larger than that of the ambient dielectric, e.g. air $n = 1$, for a surface plasmon mode is equivalent to an increase of the overall effective index integrated over the evanescent field. The net effect is a slight shift of the dispersion curve corresponding to an increase of k_{sp} for any given ω_L. This is depicted in Figure 7(*a*) (*dashed curve* labeled PSP[b]). As a consequence, the angle of incidence that determines the photon wave vector projection along the PSP propagation direction has to be slightly increased [from θ_0, point *B* on curve PSP[a] in Figure 7(*a*) and Figure 3(*b*) to θ_1, point *D* in Figure 7(*a*)] in order to again couple resonantly to PSP modes (19).

Experimentally, the situation is relatively simple as schematically depicted in Figure 7(*b*). A linearly p-polarized laser beam of wavelength λ, incident at an angle θ on the noble-metal-coated base of the prism (which is covered with the thin film of interest) is reflected, and the intensity of the reflected light is monitored with a detector as a function of θ. A typical reflectivity curve is given in Figure 7(*c*). The curve labeled *a* was taken in air on a bare Au-film evaporation-deposited onto the prism base. For $\theta < \theta_c$ the reflectivity is rather high compared to the total internal reflection discussed in Figure 1 [see Figure 1(*b*)] because the evaporated metal layer acts as a mirror with little transmission. The deposition of an ultrathin organic layer prepared by the spontaneous self-assembly process of thiol chain molecules [SH-$(CH_2)_{21}$-OH] from solution to the Au-surface results in a shift of the dispersion curve for PSP running along this modified interface and hence in a shift of the resonance angle [from θ_0 to θ_1, see Figure 7(*c*)]. The obtained reflectivity curve is labeled *b* in Figure 7(*c*). The critical angle θ_c is unaffected by the presence of the self-assembled monolayer (SAM).

For all practical purposes, the quantitative treatment of this problem is based on the Fresnel theory for calculating the overall transmission and reflection of a general multilayer assembly. The latter would, in our case, consist of the prism material, the metal layer, the organic layer(s), and the superstrate, typically air or a transparent liquid, e.g. water. Different algorithms based on either a matrix formalism or a recursion formula procedure for calculating the Fresnel coefficients of the i-th layer for s- and p-polarized light have been treated in the literature. The angular dependence of the overall reflectivity can be computed and compared with the measured curves [*full curves*, Figure 7(*c*)]. The best

fit then results in a set of parameters describing the Au reference layer and, more importantly, the optical thickness of the organic coating. If the refractive index of the material is known, the geometrical thickness can be determined, and vice versa. This ambiguity can be resolved if PSP resonance curves are taken at different wavelengths (20) (with the ambiguity of the unknown dispersion behavior of the refractive index of the coating), or in a contrast variation experiment (10) where the angular resonance shift is measured in two media of different dielectric constants ε_{di}, e.g. in air and in contact to the solvent from which the thiol monolayer was assembled. Because the angular shift $\Delta\theta_i$ is a known function of d_{layer} and of the optical contrast to the surrounding medium, $(\varepsilon_{layer} - \varepsilon_{di})$, i.e.

$$\Delta\theta_i = f(d_{layer}, (\varepsilon_{layer} - \varepsilon_{di})), \qquad 20.$$

one needs two independent measurements to separate ε_{layer} and d (21).

Guided Optical Modes

If the thickness of the coating is increased further, a new type of nonradiative mode, guided optical waves, can be observed. This is schematically illustrated in Figure 8. The excitation of these modes of different order m can be seen again if the reflected intensity is recorded as a function of the angle of incidence, θ [Figure 8(*b*)]: narrow dips in the reflectivity curve above θ_c indicate the existence of the various guided waves.

This waveguide format is a special version of the general principle of guiding light in a transparent medium with confined (optical) dimensions. The three basic configurations (22, 23) are schematically depicted in Figure 9: the planar waveguide structure [Figure 9(*a*)] given in the so-called asymmetric slab configuration with a solid substrate and a low-index material as superstrate; the various channel waveguides [Figure 9(*b*)], strip, embedded strip, and buried strip, from top to bottom prepared by starting in some cases with a planar waveguide and then further structuring and etching the sample; and the optical fiber [Figure 9(*c*)] with a high index core and a lower index cladding. Such waveguide structures are discussed in the literature not only with respect to their role as passive interconnects between different integrated optical circuit (IOC) components, but also in the context of various design concepts for active IOC modules such as directional couplers, phase and amplitude modulators, and second harmonic generators for laser diodes (24).

In the following, we first describe very briefly the basic theoretical approaches (within Maxwell's theory) needed to understand the phenomenon of guiding light in confined geometries. We limit the discussion to the case of a planar waveguide structure, but the general ideas allow for a straightforward extrapolation to more complicated designs.

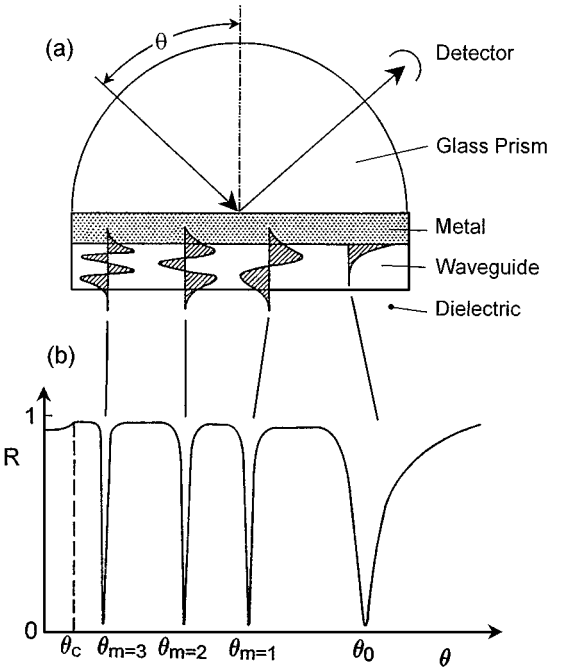

Figure 8 (*a*) Schematic of a PSP/waveguide spectroscopy combination scheme: In addition to the PSP wave, various waveguide modes can be excited by this configuration, provided the dielectric thin film (waveguide) structure is thick enough. (*b*) Excitation of these modes can be seen in the reflectivity curve as very sharp dips as one measures the reflectivity R as a function of the angle of incidence θ. Modes are indexed according to the number of nodes of their field distribution in the waveguide structure. The latter is schematically sketched in the waveguide slab; see (*a*).

We consider the asymmetric slab configuration sketched in Figure 10(*a*). The thin waveguide layer (film with index of refraction n_2 and thickness d) is bound by the substrate (n_3) and the superstrate (e.g. air $n_1 = 1$). In order to obtain total internal reflection at each interface, the waveguide material must fulfill the requirement $n_1 < n_2$ and $n_3 < n_2$. Then, in the ray optic approach (25), which we will not consider here, the light zigzags through the planar waveguide [shown schematically in Figure 10(*a*)]. Note the evanescent wave extension giving rise to the Goos-Hänchen (26) shift. Within Maxwell's theory it can be shown that for the three-layer system depicted in Figure 10(*a*), one can write the optical field in each of the media (omitting the time dependence and the propagation in the x-direction):

$$E_{1y} = A_1 e^{-k_{1z}(z-d)} \quad z \geq d \qquad 21.$$

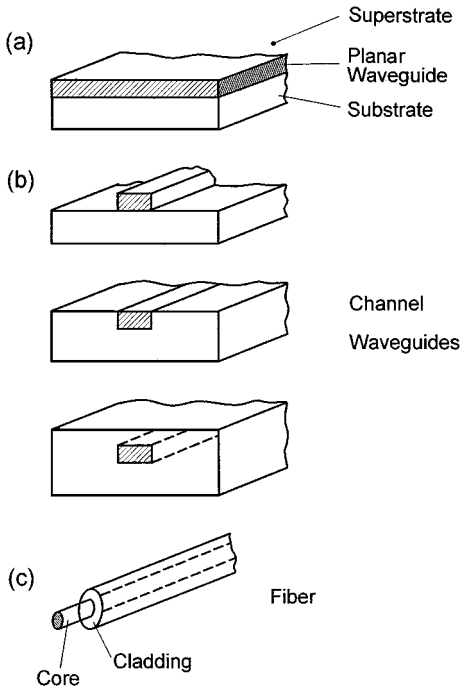

Figure 9 Basic waveguide structures: (*a*) Planar waveguide (*shaded*) on a substrate, covered by a low-index superstrate. (*b*) Channel waveguides: (*top*), strip; (*middle*), embedded strip; (*bottom*), buried strip. (*c*) Optical fiber with the core and the cladding of lower refractive index.

$$E_{2y} = A_2 \cos(k_{2z} z + \phi) \quad 0 \le z \le d \tag{22.}$$

$$E_{3y} = A_3 e^{k_{3z} z} \quad z \le 0. \tag{23.}$$

Matching both electric and magnetic fields at each interface we obtain at $z = 0$

$$A_3 = A_2 \cos\phi \tag{24.}$$

and

$$k_{3z} A_3 = k_{2z} A_2 \sin\phi. \tag{25.}$$

Therefore,

$$\phi = \tan^{-1}\beta_{23} \quad \text{with} \quad \beta_{23} = k_{3z}/k_{2z} \tag{26.}$$

and

$$A_2 = A_3\sqrt{1 + \beta_{23}^2}. \tag{27.}$$

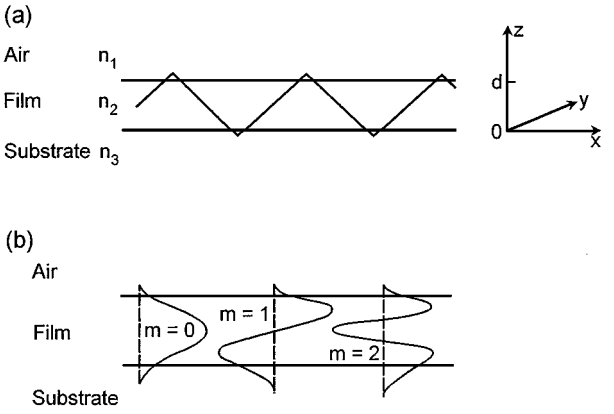

Figure 10 (*a*) The geometry of a planar waveguide with substrate (index of refraction n_3), film (thickness d, n_2), and superstrate, e.g. air (n_1). Also given is the coordinate system used to derive the mode equation. For illustration only, note the ray optic description of the guided light. (*b*) Optical field distribution in a planar waveguide structure of substrate/film/air configuration for the first three s-polarized modes ($m = 0, 1, 2$). The higher index of the substrate ($n_3 = 1.46$) compared to the superstrate (air, $n_1 = 1.0$) is the reason for the much stronger evanescent field penetrating the substrate material.

At $z = d$ one finds

$$A_1 = A_2 \cos(k_{2z} d + \phi) \tag{28.}$$

and

$$-k_{1z} A_1 = -k_{2z} A_2 \sin(k_{2z} d + \phi). \tag{29.}$$

Then

$$\phi = -k_{2z} d + \tan^{-1} \beta_{21} \quad \text{with} \quad \beta_{21} = k_{1z}/k_{2z} \tag{30.}$$

and

$$A_2 = A_1 \sqrt{1 + \beta_{21}^2}. \tag{31.}$$

The phase factor ϕ in Equations 26 and 30 must be the same within a multiple of π. Therefore, for the nonabsorbing case considered here, one arrives at the well-known eigenvalue equation for waveguide modes of order m (27):

$$k_{2z} d = \tan^{-1} \beta_{21} + \tan^{-1} \beta_{23} + m\pi. \tag{32.}$$

For a given set of materials and hence refractive index combination (which determines $\tan^{-1} \beta_{21}$ and $\tan^{-1} \beta_{23}$ for a fixed frequency) the number of eigenmodes depends only on the thickness of the waveguide layer.

The detailed analysis of Maxwell's equations can yield the optical field distribution for each eigenmode. Figure 10(*b*) shows the optical field distributions for the first three modes (with their *E*-field being parallel to the film along the *y*-axis) calculated with the following indices of refraction: (*a*) substrate $n_3 = 1.46$; (*b*) waveguide film $n_2 = 1.55$; (*c*) cladding (air) $n_1 = 1$. Note that the optical field extends as an evanescent wave into both the cladding and the substrate where it decays exponentially as a function of distance from the interface, although for this asymmetric slab in an asymmetric way.

Considering that for all guided modes this momentum along the propagation direction, k_x, is larger than that of the corresponding photon (of the identical energy $\hbar\omega$) in free space, again, one has to use a coupling device to excite waveguide modes by a laser beam. The three most important techniques for coupling light into a waveguide are schematically sketched in Figure 11. The grating [Figure 11(*a*)] and prism coupling method [Figure 11(*b*)] are commonly used for planar waveguides. Efficient coupling can be achieved only under wavevector matching conditions. For grating coupling, this requires that the photon wavevector component parallel to the surface plus or minus a multiple of the grating vector $\vec{G}$, with $|\vec{G}| = 2\pi/\Lambda$ and Λ being the groove

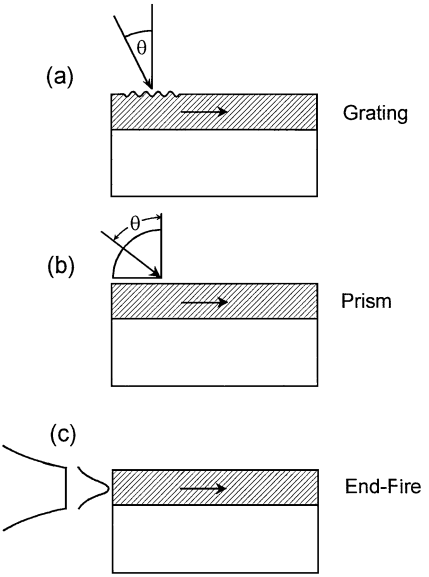

Figure 11 The three basic coupling geometries. (*a*) Grating coupling; (*b*) prism coupling; (*c*) end-fire coupling, e.g. by a microscope objective. Both (*a*) and (*b*) require the tuning of the angle of incidence θ.

spacing of the grating, match to the waveguide propagation vector

$$k_{x,m} = k_{ph} \sin\theta \pm mG. \qquad 33.$$

In the case of prism coupling, the projection of the photon wavevector at the base of the prism must be equal to the guided wavevector:

$$k_{x,m} = k_{ph} n_p \sin\theta, \qquad 34.$$

with n_p being the index of refraction of the prism. This requires a prism with an index higher than that of the waveguide material. The grating- and prism-coupling conditions for guided wave excitation are completely equivalent to the corresponding schemes described above for surface plasmon excitation.

The end-fire coupling (e.g. from a microscope objective to a channel waveguide) matches the spatial distribution of the incident field to that of the guided wave [Figure 11(*c*)].

For a given waveguide, e.g. a planar structure of fixed thickness, the number of modes and their angular positions when excited by a grating or prism (refer to Equations 33 and 34) depends on the wavelength employed and on the index of refraction of the various layers. For a thin film of an unknown waveguide material this allows for the determination of the corresponding material's parameters.

Our configuration (see Figure 8) is somewhat special in that coupling of laser light occurs through the thin metal layer as the coupling gap. In this geometry, the $m = 0$ mode is the surface mode, the surface plasmon. Its optical intensity peaks at the metal-waveguide interface and decays (for films of typical waveguide thicknesses of approximately 1 μm or more) completely within the film. Its polarization is predominantly parallel to the film normal. Its angular position, therefore, depends only on n_z, not on the waveguide thickness. The other waveguide modes can be excited with either s- or p-polarized light and will, in general, depend on all three indices—that is, n_x, n_y, and n_z as well as on the film thickness (see Equation 32). Another important feature of our setup is the fact that this geometry ensures that the guided light is constantly coupled out again through the prism so that the propagation length L_x is also reduced to a few μm. This is an important feature in waveguide microscopy (28).

SURFACE PLASMON AND OPTICAL WAVEGUIDE SPECTROSCOPY

In this section we will discuss a broad range of examples for the characterization of the structural and optical properties of thin and ultrathin films with different optical architectures. The systems investigated in air or at a solid/solution

interface range from self-assembled monolayers (SAMs) (29), to monolayers and multilayers prepared according to the Langmuir/Blodgett/Kuhn-technique (30), and include assemblies fabricated by the alternate deposition of polyelectrolytes (31), electropolymerized layers (32), or films prepared simply by the spin-coating technique.

Thickness Determination

One of the classical techniques used for the fabrication of ultrathin coatings is based on the preorganization of amphiphilic molecules like fatty acids, lipids, and the like at the water/air interface, typically in a Langmuir trough (33, 34). After spreading from a volatile organic solvent, these water-insoluble molecules are compressed to the desired packing density by a movable barrier in the trough and are then transferred to a solid support by dipping and withdrawing the substrate through the monolayer-covered water surface (35). The number of dipping cycles determines the number of layers transferred, and hence allows a molecular control of the overall film thickness.

The system that we first discuss as an example for the use of PSP resonance to analyze thin films is based on LBK multilayer assemblies prepared from polyglutamate monolayers (36). These materials were recently introduced as novel polymeric systems that can be processed by the LBK technique and that allow the buildup of very homogeneous thin film coatings. A schematic drawing of a transferred double layer is presented in Figure 12(*a*). It shows the quasi-two-dimensional nematic structure of these "hairy rods"—called stiff polyglutamate helices—with long, flexible alkyl sidechains.

Figure 12(*b*) gives the results of ATR scans obtained from the bare metal and 2, 4, 6, 10, and 20 layers of polyglutamate, respectively. All these layer preparations can be described by a constant index of refraction $n_z = 1.486$ and the multiple of a constant thickness per monolayer of $d_0 = 1.75$ nm.

As mentioned already, the mere surface plasmon resonance curves would not have allowed us to separate the refractive index and thickness of the layers. However, the simultaneous recording of X-ray reflectometry scans gave independent information as to the electron density profile of the coatings normal to the surface from which the geometrical thickness of the layers could be derived (37). Moreover, for thicker films capable of carrying a guided optical mode, a separation of n and d was possible; see below.

For the purpose of modifying surface properties of solids, a very attractive alternative to transferred Langmuir monolayers is monomolecular films prepared by a self-organization process. Suitable substrates are immersed in a solution that contains the surface-active molecules. These then self-assemble at the solid/solution interface to a well-organized monomolecular layer with a structural (positional and orientational) order comparable to Langmuir films.

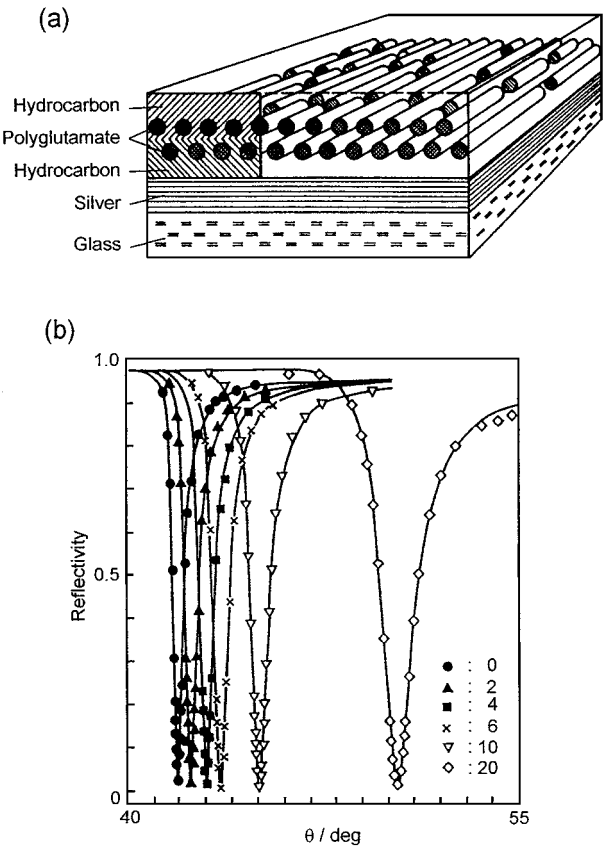

Figure 12 (*a*) Schematic drawing of the architecture of the thin film: 50 nm Ag is evaporated onto the glass prism and a double layer of polyglutamate is laid down by the Langmuir-Blodgett-Kuhn technique. The long oriented rods are the polypeptide α-helices. Hydrocarbon represents the disordered alkyl sidechains. (*b*) Reflected intensity ($\lambda_L = 633$ nm) as a function of the angle θ for various film architectures. *Solid circles*, bare Ag ($\varepsilon_{Ag} = -16.35 + i0.6$, thickness $d = 50.8$ nm); *solid triangles*, two layers of polyglutamate on top; *solid squares*, four layers of polyglutamate on top; *crosses*, six layers of polyglutamate on top; *open triangles*, ten layers of polyglutamate on top; *diamonds*, 20 layers of polyglutamate on top. *Solid lines*, Fresnel calculations.

The first examples, introduced by Sagiv in 1980 (38), were based on the specific interaction between the silyl-headgroup of the amphiphiles (e.g. of octadecyltrichlorosilane) and the polar silanol groups on glass or quartz substrates. More recently, a major research activity has focused on the physics and chemistry of SAMs based on the interaction of thiol, disulfide, and sulfide groups with Au and Ag surfaces. The possibility for chemical manipulations at the ω-position of long-chain thiols [X-$(CH_2)n$-SH with X: functional group] opened a wide field

of tailormade surface functionalizations. This molecular engineering of surface properties has wide implications for lubrication, patterning, (bio)-sensing, cell-surface engineering, and so on.

The structural formula of one example of functional molecules that can form SAMs on glassy surfaces is presented in Figure 13(*a*), and shows the triethoxysilane unit that can accomplish the covalent and hence stable binding to the glass substrate (39). The alkyl chains and the attached chromophores play the role of the hydrophobic tails of "classical" amphiphiles. In practice, azo-silane SAMs for the PSP experiments [Figure 13(*b*)] were prepared as follows: After the cleaning procedure, the glass substrates were dried in an oven at 120°C before being coated with Ag (53 nm) and SiO_2 (18 nm). To enhance the surface coverage of hydroxy groups, these substrates were then immersed in potassium hydrogen phosphate buffer (0.1 M, pH 9.4) for 30 min, rinsed thoroughly with ultrapure water (Milli-Q), and dried in an oven at 120°C . The silanization process was achieved by immersing these treated substrates in a 0.5% solution of the azo-silane in ethanol for 10 min, rinsing with dichloromethane and ethanol, and subsequent baking in an oven at 120°C for 2 h. Two substrates were not placed in the silanating solution (although they were subject to the treatment stated above) and were kept for use as reference samples in the PSP experiments [refer to Figure 13(*b*), *full circles*]. The samples were then stored in a sealed vessel prior to the experiments.

Figure 13(*b*) gives the angular scan (*open circles*) of the PSP resonance found for our SAM; the *full line* is a theoretical fit from Fresnel calculations. The angular shift of the resonance can be well described by assuming for the SAM a refractive index of $n_{layer} = 1.50$ and a thickness of $d = 0.9$ nm. Irradiating the sample with UV light (360 nm) shifts the dark-adapted all-*trans* chromophores through *trans* $\rightarrow$ *cis* isomerization to a photostationary equilibrium with a high *cis* isomer content. As a result, the optical refractive index anisotropy is changed and the index normal to the layer is reduced. This shifts the surface plasmon resonance to smaller angles, corresponding to a SAM layer that is optically thinner. However, this shift is too small to be seen by the naked eye (see, however, the kinetic mode described below: Figure 34).

The third example of ultrathin coatings that we present concerns the formation of polymeric multilayer assemblies by a protocol recently introduced by Decher and Hong (40). A charged substrate is sequentially exposed to solutions of cationic and anionic polymers resulting in the adsorption of very stable polymer films the thicknesses of which are controlled at the nm level by the number of deposition cycles. Our experiments used a modified version of the preparation procedure that allowed for the on-line control of the polyelectrolyte deposition in a flow cuvette (41). Figure 14(*a*) gives a schematic representation of the setup: We deposited one monolayer of the positively charged amphiphilic ionene (compound 1) [see Figure 14(*b*)] onto the glass (high index,

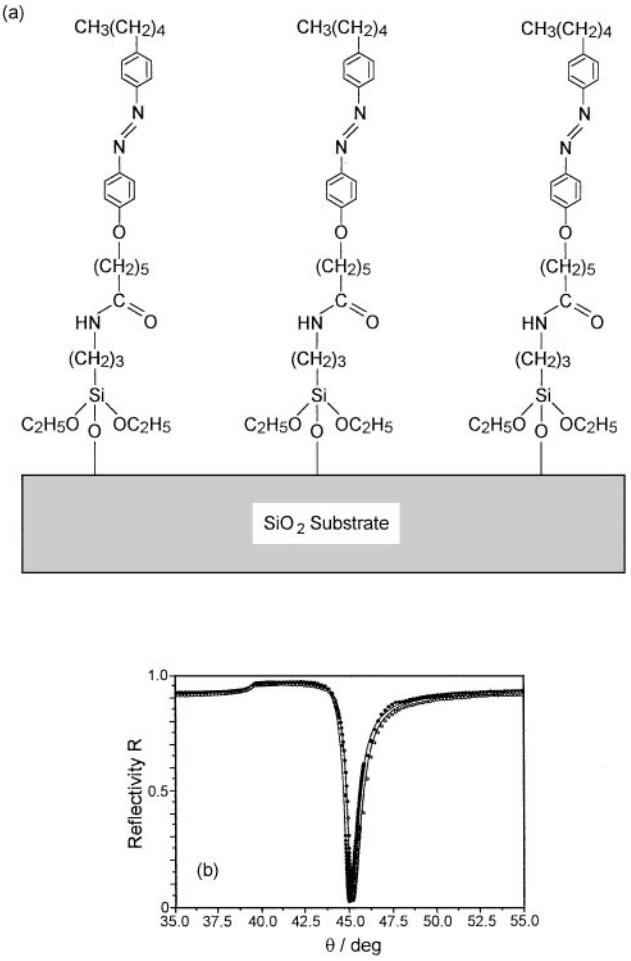

Figure 13 (*a*) Structural formula of 4-[6-carboxy-(3-amidopropyl)triethoxysilane]-4′-pentyl-azobenzene, referred to in the text as azo-silane, that leads to a self-assembled monolayer. Depicted is an idealized schematic drawing of a SAM on a SiO_2 substrate. (*b*) PSP resonance of the bare Ag substrate (*closed circles*) and after coating with a self-assembled monolayer, the azo-silane (*open circles*); the *full curves* are Fresnel fits with the following thicknesses: $d_{Ag} = 53.4$ nm, $d_{SiO_2} = 18.4$ nm, $d_{SAM} = 0.9$ nm.

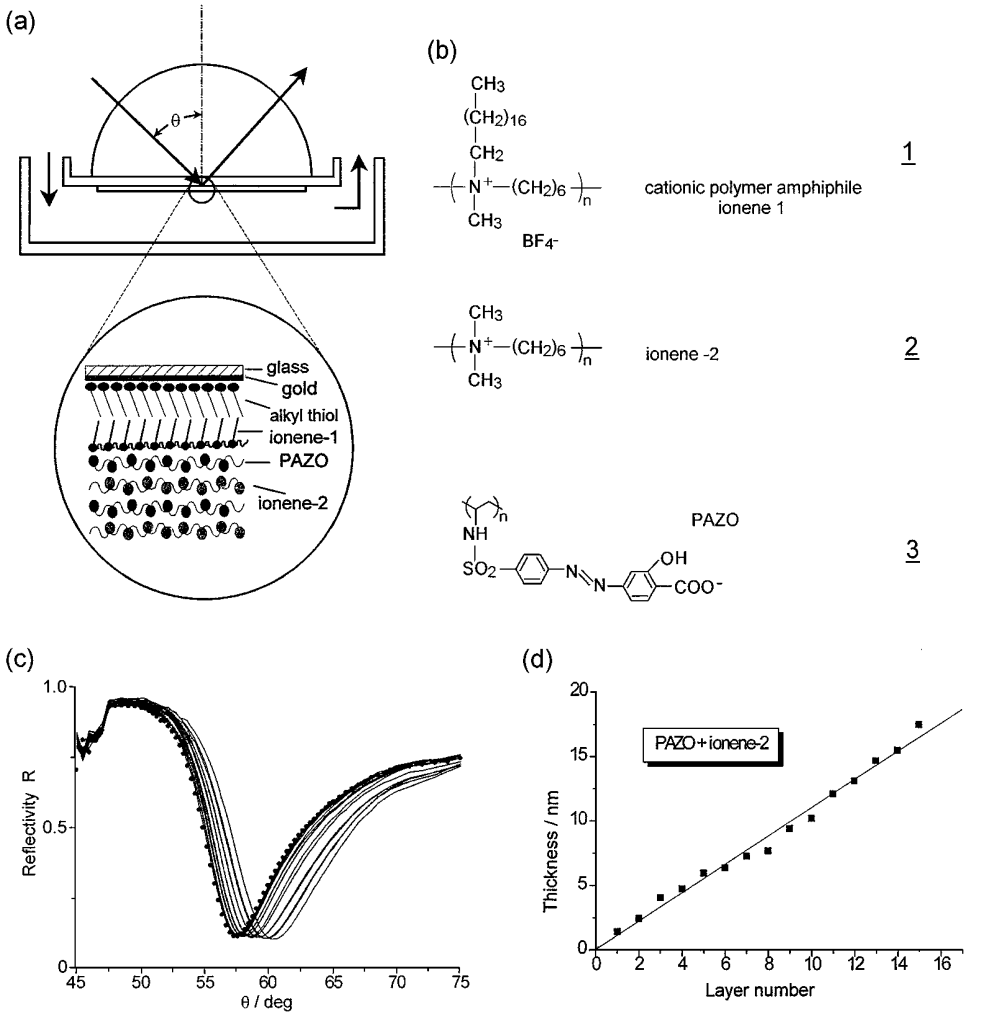

Figure 14 (*a*) Experimental construct for on-line surface plasmon optical observation of the alternating deposition of cationic and anionic polymers from solution to an Au substrate precoated by an alkyl thiol and an ionene-1 monolayer [refer to (*b*)]. The build-up architecture is given in the enlargement. (*b*) Structural formulas of the employed materials. (*c*) Series of ATR scans taken after each polyelectrolyte monolayer deposition. (*d*) Thickness increase as obtained from the ATR scans given in (*c*).

LaSFN9, $n = 1.85$ @ $\lambda = 633$ nm)/Au/octadecyl-thiol layer sandwich in the Langmuir trough during the downstroke of the LBK process. The sample was then mounted to the flow cell under water [see Figure 14(*a*)], to keep the charged ammonium head groups of the ionene polymer in constant contact with the electrolyte solution. The angular scan of this reference surface is given in Figure 14(*c*), *full circles* (note the large coupling angle which is due to the fact that all data were taken with the surface being in contact with electrolyte solution). The first polymer solution, PAZO (compound 3) [structural formula given in Figure 14(*b*)], was injected into the cell and the polyelectrolyte allowed to adsorb with its negative charges to the positive groups of the solid interface. A period of 15 min was found to be sufficient for stable monolayer formation (see also the kinetic data presented below, Figure 19, for another polyelectrolyte adsorption) and the corresponding plasmon resonance scan was taken. After careful rinsing with pure buffer (which had no net effect on the adsorbed polyelectrolyte layer thickness), the positively charged ionene-2 [see Figure 14(*b*)] was injected and allowed to adsorb, again for 15 min. The angular scan was recorded, and the procedure repeated several times. As a result, a multilayer assembly of alternating polymers was obtained with opposite charges as sketched in Figure 14(*a*).

A sequence of raw reflectivity data taken after consecutive depositions is shown in Figure 14(*c*) as *full curves*, each shifted relative to the one taken before. The net angular shift per deposition is relatively small so that some fluctuation in the sequence of reflectivity scans is obvious. Nevertheless, a Fresnel analysis based on a refractive index of the layers of $n = 1.50$ gives an effective thickness increment per layer, which results in a linear increase of the multilayer thickness as shown in Figure 14(*d*). A closer inspection of the data points reveals that the odd-numbered depositions corresponding to the PAZO adsorption gave a larger thickness increase of $\Delta d = (1.55 \pm 0.27)$ nm, whereas the even-numbered ones obtained with the ionene-2 solution gave only $\Delta d = (0.63 \pm 0.3)$ nm. From the slope of the least-squares fit shown in Figure 14(*d*), one obtains an average thickness increase per double layer deposition of $\Delta d = 2.18$ nm.

Because of the evanescent character of surface plasmons, recording reflectivity scans in the Kretschmann configuration was easily possible at this solid/solution interface as well. The setup had to be modified only to allow for the installation of a liquid cell and thus proved to be a very versatile tool in characterizing the optical properties of thin polymer films (42).

As we pointed out in the preceding section, a more detailed analysis of the optical properties of organic thin layers is possible, if their thickness is large enough to allow for the excitation of at least one guided mode in each p- and s-polarization. For the polyglutamate multilayer assemblies introduced in Figure 12, this required the deposition of 150 layers. As can be seen from

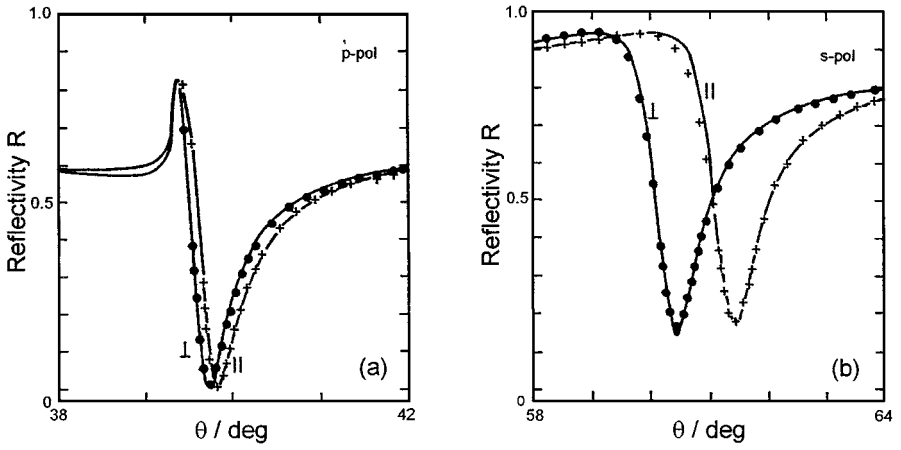

Figure 15 Reflectivity vs angle-of-incidence scans for a thick (150 layers) polyglutamate LBK film on a Cr/Au layer in a Kretschmann configuration with (*a*) p-polarization (*TM*) and (*b*) s-polarization (*TE*). Both scans were performed with the mode propagation direction parallel (||) or perpendicular ($\perp$) to the rod axes (dipping direction). *Solid circles* and *crosses* are experimental points; *solid lines* are Fresnel calculations. The laser wavelength was $\lambda_L = 633$ nm.

Figure 15, this resulted in an easily observable s-mode, and the corresponding p-mode ($m = 1$) just became visible beyond the critical angle θ_c (36). This figure directly demonstrates the optical in-plane anisotropy of these films, which can be more sensitively probed with s-polarized light. Note the high sensitivity of the TE modes for such subtle index anisotropies.

If the waveguide layer is thick enough and if the index of refraction of the coupling prism is high enough, (Equation 2), then a surface plasmon can be excited that decays completely within the waveguide material and hence is sensitive only to its index of refraction but not to its thickness. This case, schematically included in Figure 8, demonstrates that a very sensitive self-consistent analysis of the different guided modes leads to a rigorous evaluation of the (anisotropic) optical properties of laterally homogeneous thin polymeric coatings.

The last example that we describe concerns one of the best waveguide samples experimentally available: the nearly perfect plane slab of a mica sheet (43). Mica recently attracted general interest as a substrate material that can be easily rendered atomically flat and chemically very clean by simply cleaving the upper layers. The flat surfaces thus obtained are used in scanning (atomic) force microscopy (AFM) (44) and in the surface forces apparatus (SFA) (45). In the latter application, the back side of the thin mica sheet is coated with a semitransparent Ag layer and then glued onto the semicylindrical quartz discs as part of the multipass interferometer used to measure the separation distance

between the two surfaces of the upper and the lower disc. We adopted this preparation procedure for the excitation of optical modes guided within the mica slab: The Ag- or Au-coated mica sheet was glued to a coupling prism, and after a final cleavage of the upper atomic layers mounted to a flow-cuvette in a surface plasmon/waveguide spectrometer [see Figure 16(*a*)]. The waveguide mode spectra obtained by monitoring in air the reflectivities for s- and p-polarized excitation, respectively, are given in Figures 16(*b*) and (*c*). The very narrow resonances of this multimode waveguide that can be simulated nearly perfectly allow for a highly accurate determination of the thickness of the mica sheet and its indicatrix [refer to the Fresnel calculations (*full curves*) in Figures 16(*b*) and (*c*)]: We obtain $d_{mica} = 1921.9$ nm, $\varepsilon'_x = 2.5660$, $\varepsilon'_y = 2.5634$, $\varepsilon'_z = 2.4444$. The small imaginary part introduced for the y-component $\varepsilon''_y = 0.00035$ to match the minimum reflectivity of the high angle mode of the s-polarization at $\theta = 67$ deg [refer to Figure 16(*b*)] accounted for residual imperfections of this slab waveguide originating from terrace steps and internal mechanical stress unavoidable in the gluing process.

If this mica sheet is attached to a high index prism and further cleaved in situ, a single-mode waveguide capable of guiding one s- and one p-polarized mode is obtained. The corresponding reflectivity spectra are given, together with their Fresnel fits, in Figure 17(*a*). For illustration, two corresponding optical intensity distributions are given in Figures 17(*b*) and (*c*), respectively. Note that the mica sheet in this case was only $d \approx 320$ nm thick.

The potential of this sample/substrate format lies in the fact that the sensitivity of the angular position of the waveguide modes with respect to thin coatings is comparable to that found in surface plasmon optics. With mica, however, one is dealing with a molecularly flat surface that allows for the characterization of interfacial architectures and processes without interfering effects that result from roughness. Moreover, these optical studies complement information obtained with the SFA from thin film samples of the same structure, organization, and order. With the AFM, even combination modes of operation are feasible by correlating the laterally averaged information about the optical thicknesses with the zoomed-in data of the AFM. An example for the characterization of an interfacial binding reaction monitored with a mica waveguide mode is presented further below (refer to Figure 22).

Figure 16 (*a*) Experimental configuration used to excite waveguide modes in a thin mica sheet. A typical waveguide mode pattern is given in (*b*) for s-polarized light, (*c*) for p-polarized excitation @$\lambda = 633$ nm. *Open circles*, data points; *full curves*, Fresnel calculations with the following parameters: $\varepsilon_{prism} = 2.295$; $\tilde{\varepsilon}_{Ag} = -16.3 + i \cdot 0.6$, $d_{Ag} = 54$ nm, mica: $\varepsilon'_x = 2.5660$, $\tilde{\varepsilon}_y = 2.5634 + i \cdot 0.00035$, $\varepsilon'_z = 2.4444$, $d = 1921.9$ nm.

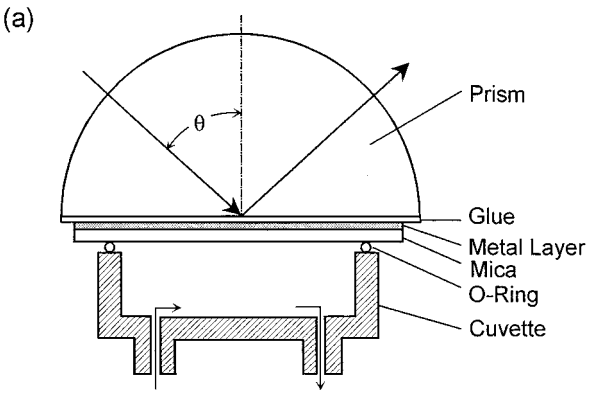
(a)
θ
Prism
Glue
Metal Layer
Mica
O-Ring
Cuvette

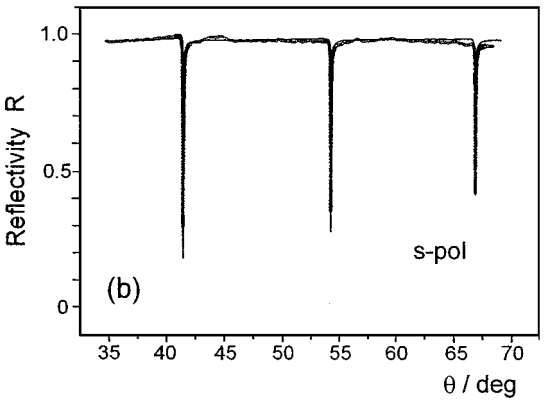
Reflectivity R
1.0
0.5
0
(b)
s-pol
35
40
45
50
55
60
65
70
θ / deg

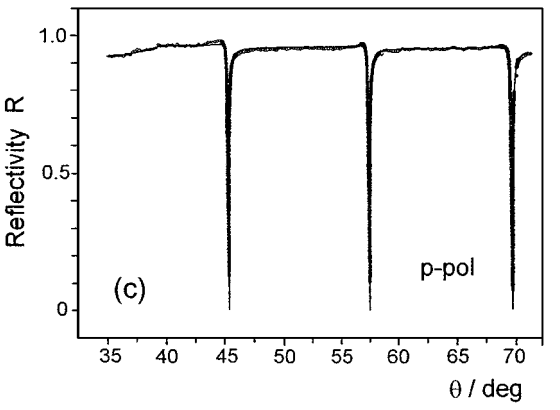
Reflectivity R
1.0
0.5
0
(c)
p-pol
35
40
45
50
55
60
65
70
θ / deg

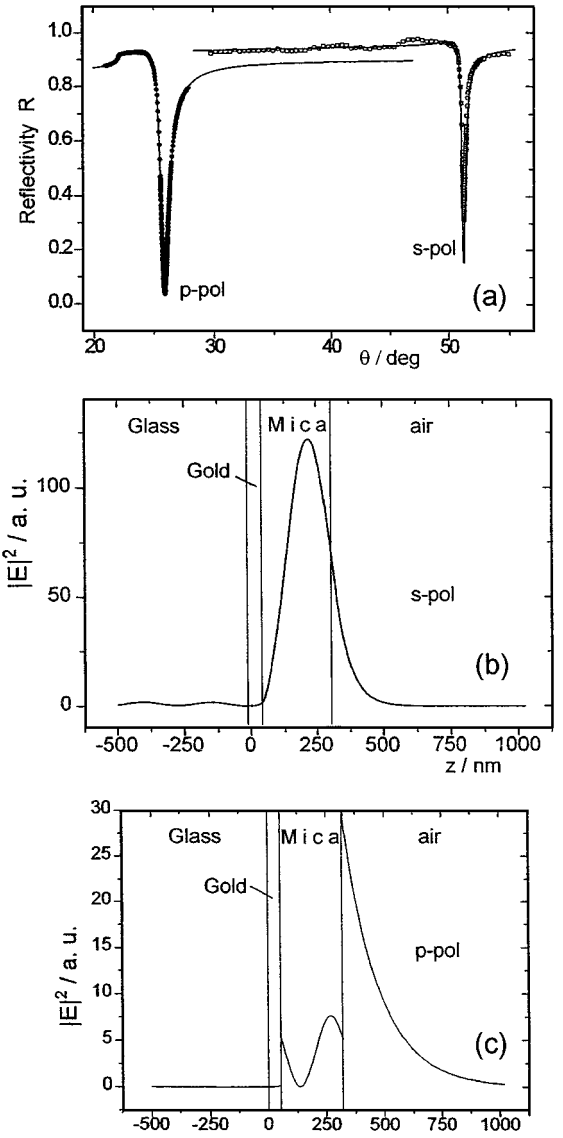

Figure 17 (*a*) Waveguide spectra @ $\lambda = 633$ nm in air using a high index prism. *Full circles*, p-polarized excitation; *open circles*, s-polarization. *Full curves*, Fresnel calculations with: $\varepsilon_{prism} = 3.4036$; $\tilde{\varepsilon}_{Au} = -12.8 + i \cdot 1.25$, $d_{Au} = 53$ nm; mica, $\varepsilon'_x = \varepsilon'_y = 2.584$, $\tilde{\varepsilon}_z = 2.465$, $d = 269.5$ nm. (*b*) Distribution of the optical field intensity, $|E|^2$, normal to the surface for the s-mode guided in a $d = 320$ μm thick mica layer. (*c*) as (*b*), but for the mode excited with p-polarization.

Kinetic Information About Interfacial Processes

The examples given so far were concerned with the (optical) thickness determination of thin film coatings of various interfacial architectures. In many cases, the recording of the film formation process itself is of interest; in others, the disassembly of the surface layer, or any time-dependent changes of its optical properties without changes in its geometrical dimensions is the focus. For many physicochemical or biophysical questions, the observation of interfacial processes at a solid substrate in contact with an aqueous medium is required. In cases where electrochemical experiments are to be performed, surface plasmon optics, particularly in the Kretschmann configuration, offer the advantage of being easily combined with the on-line recording of the electrical properties of the interfacial layer. A schematic of such a combination mode set-up is given in Figure 18(*a*). The metal layer at the base of the coupling prism needed to carry the surface plasmon mode doubles as the working electrode in a classical three-electrode electrochemistry cell attached to the prism along with the reference and counter electrode [refer to Figure 18(*a*)]. This allows for the simultaneous observation of optical and electrochemical properties of the substrate/electrolyte interface. Various modes of operation are possible: the usual reflectivity scan, R-vs-θ, [refer to Figure 18(*b*)] gives the optical thickness of any coating, as discussed. If the reflected intensity at a fixed angle of observation, θ_{obs}, is monitored as a function of time, kinetic information about any changes of the interfacial architecture can be monitored and analyzed [Figure 18(*c*)]. Such time-dependent processes could be induced by a potential sweep, and the combination set-up allows one to simultaneously record the reflectivity $R(t)$ and the flow of charges through the electrical circuit, e.g. a classical cyclic voltammogram [refer to Figure 18(*d*)].

The first example of the kinetic mode that we present refers to the adsorption of polyelectrolytes from solution to a charged interface. As demonstrated already in Figure 14, the alternation of this procedure between the adsorption of polyanions and polycations results in the buildup of multilayers. Surface plasmon optics allow for the on-line control of their film architecture while being still in contact to the aqueous medium (46). Figure 19 gives an example of the adsorption of polyaniline (compound 4) alternating with the adsorption of sulfonated polyaniline (compound 5). These layers were recently introduced as polymeric conducting coatings with a molecular thickness control. It was also shown that they enhance the performance of electroluminescent devices, when used as hole injection/transporting layers deposited onto the ITO-electrode prior to the spin-coating of the emissive layer (46). The structural formulas of the employed materials are given in Figure 19(*a*).

The time dependence of the adsorption process of sulfonated polyanaline (compound 5) onto a surface coated with polyaniline (compound 4) is given

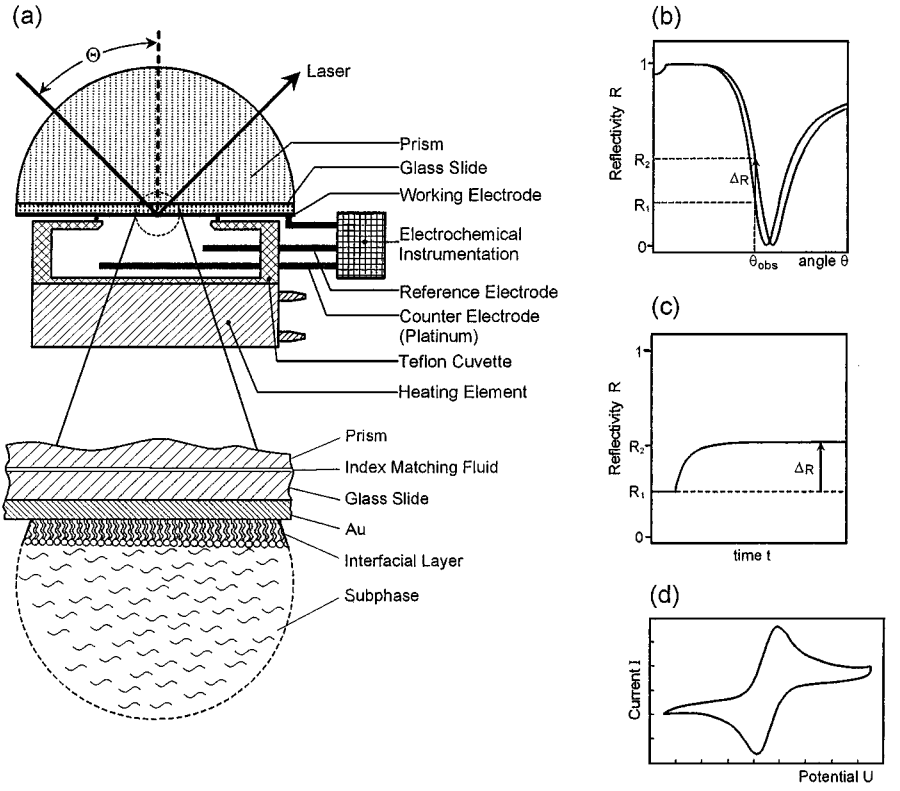

Figure 18 (*a*) Combined surface plasmon optical/electrochemical methodology used for simultaneous structural and functional characterization of interfacial layers. *Right panel*, schematics of (*b*) angular scans of surface plasmon spectroscopy; (*c*) the corresponding kinetic mode, i.e. recording the reflected intensity at a fixed angle of incidence as a function of time; (*d*) cyclic voltammetry as one example for electrochemical investigations.

in Figure 19(*b*). At $t = 0$ the aqueous solution of compound 5 ($c = 2$ mM at pH $= 3$) was injected into the liquid cell and the adsorption followed in real time as a change in reflectivity. The adsorption process is complete after several minutes, thus giving important information regarding the sequence of the alternation of the process for the multilayer preparation.

The next examples are related to the functionalization of solid surfaces by the formation of a monolayer coating in a self-organizational approach. In particular, the SAM formation from thiol derivatives on Au electrodes has attracted much interest. As shown above, PSP optics are a very sensitive tool to monitor layer thicknesses [see also Figures 7 and 13(*b*)], but can also be used to derive direct information on the monolayer assembly process.

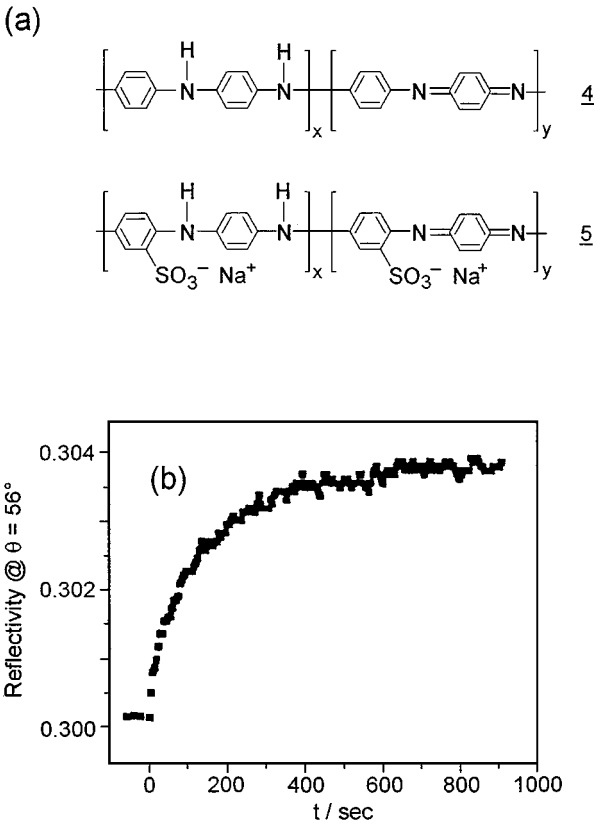

Figure 19 (*a*) Structural formulas of the polyelectrolytes used for multilayer formation by alternate deposition from solution. (*b*) Kinetic scan taken during the adsorption of sulfonated polyaniline (compound 5) onto a surface coated with polyaniline (compound 4).

The system introduced in Figure 20 was the result of our strategy to optimize the interfacial architecture as a binding matrix for the formation of a protein monolayer by adsorption from the surrounding aqueous medium (47, 48). As a model system we choose the "ligand" biotin with its very high affinity to bind to the protein streptavidin ($K_a = 10^{-15}$ M). As it turned out, maximum protein binding could be observed for a binary mixed SAM composed of 10 mole% of the biotin-thiol-derivative (compound 7) embedded into an inert matrix of 90 mole% of the diluent thiol [compound 6, structural formulas given in Figure 20(*a*)] (49). Both compounds are water-soluble and were assembled from a 10^{-4} M aqueous binary solution. When injected into the cell [*arrow*, Figure 20(*b*)], a rapid rise in the reflected intensity (diffusion-controlled) could

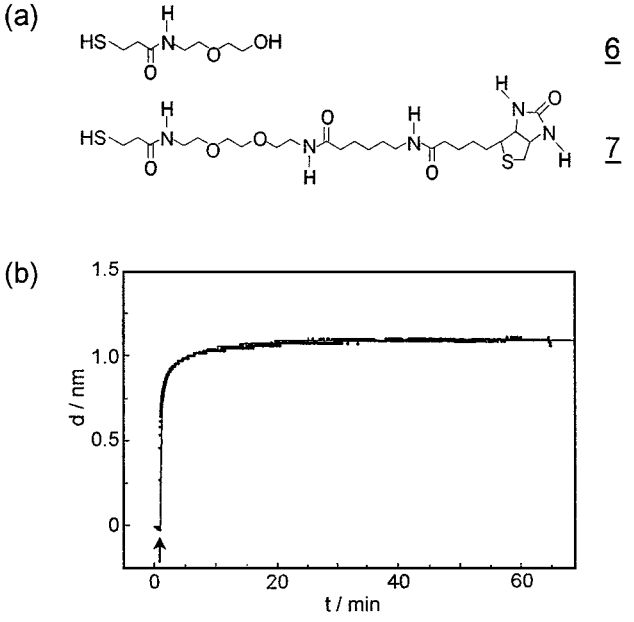

Figure 20 (*a*) Structural formula of water-soluble thiol molecules with different end group functionalities, i.e. -OH (compound 6) and -biotin (compound 7), respectively. (*b*) Thickness increase as a function of time of a binary mixed monolayer composed of thiols (compounds 6 and 7), see (*a*). *Arrow*, addition of thiol solution.

be converted into a measure of the average effective thickness increase of the layer as a function of time. This is shown in Figure 20(*b*).

The reflectivity-thickness conversion is based on the assumption of a (time-independent) refractive index of the coating, which could be wrong. Averaging the lateral structural details of any coating over the propagation length L_x (refer to "Plasmon Surface Polaritons at a Noble Metal/Dielectric Interface," above) of the PSP mode, which is on the order of a few (10) μm, obscures any details of the growth mode of the SAM. In fact, it has been shown by AFM (44) and STM (50) studies that for many thiol systems, a mechanism for the nucleation of critical SAM domains operates at early stages of the layer formation, and that at later stages these domains grow laterally and merge to finally completely cover the substrate with a continuous layer. The size of these domains (in the sub-μm range), of course, cannot be resolved by surface plasmon optics. Hence the fractional monolayer thickness given in Figure 20(*b*) has to be interpreted as the mean thickness of a heterogeneous coating composed of SAM patches (with the same refractive index and thickness as the final monolayer) and free

substrate areas. An equivalent picture would be given by plotting instead of the thickness *d*, the coverage, varying between 0 and 1, as a function of time.

Once the monolayer formation was completed, the liquid cell was rinsed, and the capacity of this functionalized surface for specific protein binding was tested. We discuss the corresponding data as they were obtained by two different experimental formats, i.e. by using a grating coupler for PSP excitation, and by waveguide spectroscopy (in a kinetic mode) with mica as the guiding material.

Figure 21 summarizes the data recorded by the grating coupling scheme. The experiments were done at a laser wavelength of $\lambda = 632.8$ nm with a grating constant of $\Lambda = 499$ nm. The gratings were fabricated in our clean room (class 100) by exposing a photoresist deposited onto a glass substrate to the hologram of two coherent expanded HeCd laser beams ($\lambda = 441.6$ nm), interfering in the plane of the resist layer. After development, surface corrugation was transferred into the glass by reactive ion etching with a mixture of CF_4, C_2F_6, and O_2. After evaporation coating the glass grating with approximately 150 nm of Ag, the substrate could be mounted into a liquid cell, allowing for the excitation of PSP modes at the aqueous interface.

The combination of the grating constant Λ, the laser wavelength λ, and the dielectric constant of water, ε_{H_2O}, resulted in an experimental configuration for which one operates on the third branch of the dispersion curve [refer to Figure 6(*b*)] (51). Any coating with $\varepsilon_{layer} > \varepsilon_{H_2O}$ hence results in a shift of the resonance angle to higher values. This is shown in Figure 21(*a*). The grating substrate was a special preparation in that, first, 150 nm Ag were evaporated, and then 5 nm of Au were deposited on top. This way, the optical properties of the metal, in particular, ε_m'', were largely determined by the silver, whereas the SAM formation took place at a surface which was dominated by Au. The reference reflectivity scan of this grating in contact to H_2O is the curve (labeled *1*) in Figure 21(*a*). After the formation of a binary mixed thiol SAM composed of thiols (compound 6 and compound 7), the angular shift of the next curve (labeled *2*) was observed. The kinetic data presented in Figure 21(*b*) were obtained by recording the reflectivity at $\theta_{obs} = 8.5$ deg as a function of time. After injection of streptavidin [*arrow*, Figure 21(*b*)] a rapid rise of the reflectivity indicates the shift of the resonance to even higher angles caused by the protein monolayer formation via binding of streptavidin to its "ligands" biotin. If this shift is converted again to thickness values, we find a final protein layer of $d = 4$ nm thickness. The final corresponding angular scan taken after the completion of the binding process and rinsing of the cell is given in Figure 21(*a*, curve *3*). The experimental data can be described well by a theoretical curve calculated with a Rayleigh treatment of the grating coupling scheme (52, 53).

This example gives evidence that, indeed, grating couplers can also be used for recording bio-recognition events at functionalized solid/liquid interfaces

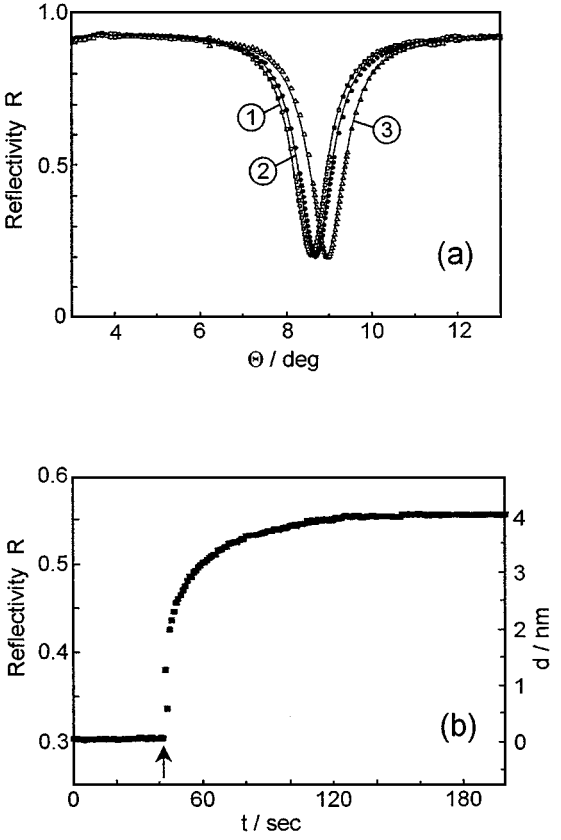

Figure 21 (*a*) Angular reflectivity scans: 1. of a bare Ag/Au-grating in water; 2. after deposition of a binary mixed thiol-SAM; 3. after the formation of a streptavidin monolayer by specific binding to the biotin ligands in the SAM. The experimental data can be well described by a Rayleigh treatment of the excitation of PSP modes by the grating structure. (*b*) Kinetic data, i.e. reflectivity at $\theta_{obs} = 8.5$ deg as a function of time after injection of streptavidin (*arrow*) into the liquid cell in contact to the thiol-SAM coated grating.

on-line. This might be relevant for optical sensor formats with surface plasmon light, because gratings as coupler elements would not need the use of an external prism, and could be rather cheap disposable chips if fabricated, i.e. by embossing a master grating into a polymer substrate.

The other example of the binding of streptavidin to a functionalized surface is based on mica as a slab waveguide substrate. The relatively inert chemical surface of mica requires different strategies to functionalize the optical device,

e.g. for optical biosensor application. The scheme that we used was identical to the one reported for the preparation of interfacial membrane architectures in studies with the SFA (54). First, a densely compressed Langmuir monolayer of the phospholipid DPPE (compound 10) was transferred from the water/air interface to the mica layer which was Ag-coated on the backside and then glued to the quartz disks of the SFA (refer to Figure 16). This hydrophobic substrate was then coated horizontally by the Langmuir/Schäfer technique with a lipid monolayer composed of 95 mole% of the fluid phospholipid DLPE (compound 8) (structural formula given in Figure 22(*a*)], doped with 5 mole% of the biotinylated phospholipid DPPE (compound 9) [structural formula also given in Figure 22(*a*)]. A schematic cartoon of the functionalized interfacial membrane thus obtained is given in Figure 22(*a*).

If the reflected intensity is recorded at a fixed angle of incidence near one of the waveguide resonances, the injection of streptavidin at $t = 0$ leads to the kinetic binding curve given in Figure 22(*b*): a fast initial rise merges into a plateau region of constant reflectivity for longer time ($t > 20$ min). If this intensity change is converted to an average thickness increase, the obtained values nearly quantitatively agree with the data presented in Figure 21(*b*) and indicate the formation of a complete monolayer of streptavidin bound to the biotinylated headgroups of the lipid layer.

Figure 22(*c*) gives evidence that, indeed, the early rise of the binding curve is diffusion-controlled: If the thickness increase is plotted as a function of $\sqrt{t}$, implying a diffusional process, a straight line is obtained after a certain initial time lag because of the injection and mixing of the streptavidin (StA) solution. From the slope of the straight line, $\frac{\partial d}{\partial \sqrt{t}}$, the diffusion coefficient, D, can be derived according to

$$D = \frac{\pi}{4}\left(\frac{\partial d}{\partial \sqrt{t}} \cdot \frac{(n_{StA} - n_d)}{\partial n / \partial c_{StA}} \cdot \frac{1}{c_{StA}}\right)^2, \qquad 35.$$

with c_{StA} = streptavidin concentration; $n_{StA} = 1.45$; $\partial n/\partial c_{StA} = 0.212$ ml/g, the refractive index increment for streptavidin solutions. We obtain $D = 2 \cdot 10^{-7}$ cm^2/s, which is in the reported range for proteins in aqueous solutions.

The next example concerns the electrochemical control of surface functionalization by electrochemical processes. The observation of the reductive desorption of chemisorbed thiol layers (55, 56) and their oxidative readsorption (57) paved the way for a new strategy to functionalize sensor spots in a matrix array selectively and individually (18).

This can be demonstrated convincingly by the combined electrochemical/surface plasmon optical set-up given in Figure 18. An example based on surface plasmon spectroscopy is summarized in Figure 23. First, a monolayer of thiol

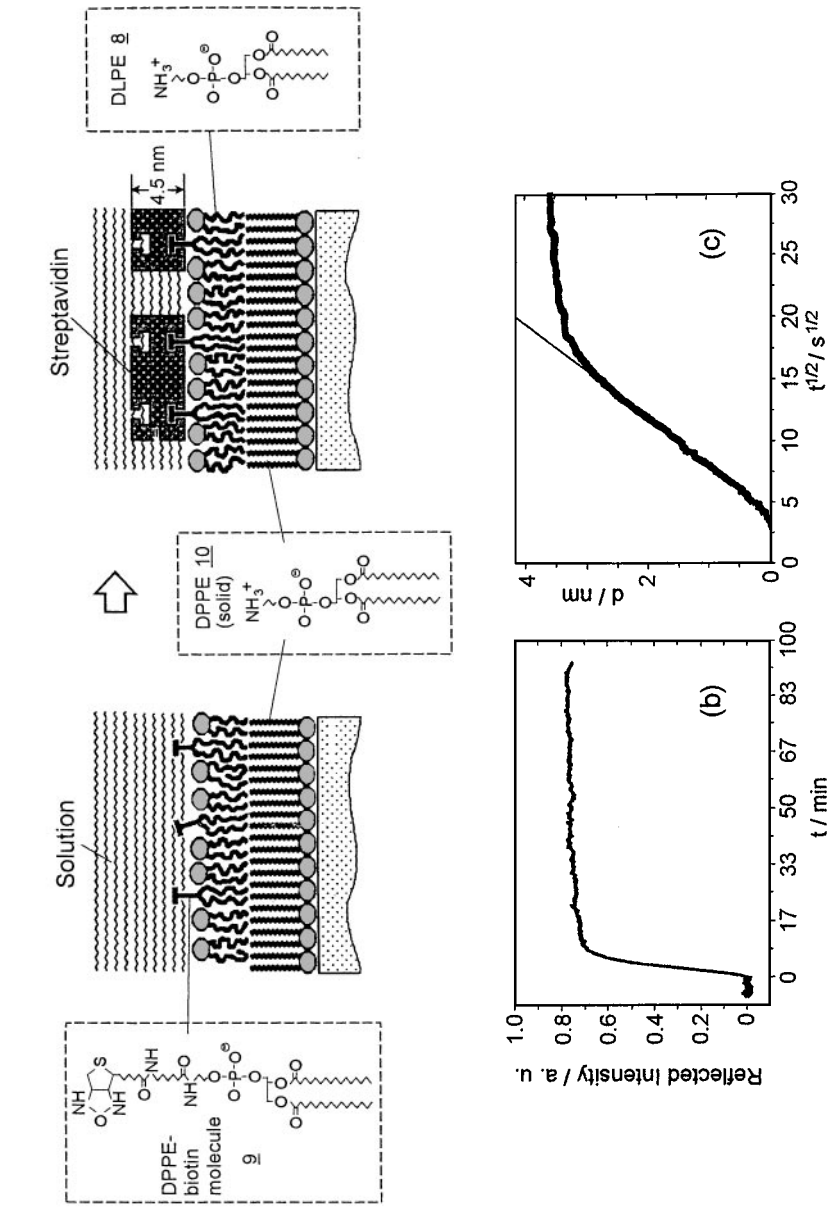
(a)
Solution
DPPE-biotin molecule 9
DPPE 10 (solid)
Streptavidin
4.5 nm
DLPE 8
(b)
Reflected Intensity / a. u.
t / min
(c)
d / nm
t^1/2 / s^1/2

(compound 6) was assembled in an aqueous 0.10 M KOH solution. The working electrode was the 50 nm thick Au-layer evaporated onto a high index LaSFN9 substrate. The potential was then cycled at a constant scan rate of 20 mV/s from -0.10 V to -1.2 V and back to -0.1 V. The corresponding current is given in Figure 23(*a*). The two cathodic waves typical for polycrystalline Au surfaces with at least two thiolate populations of different binding strengths are clearly seen: The onset potential for the first reductive current is at $U \approx -0.86$ V, with a peak potential of $U = -0.93$ V, and a second, broader peak at $U = -1.04$ V. Because we are dealing with water-soluble thiol molecules, no significant anodic wave is found, indicating no oxidative readsorption. Consequently, the second cathodic scan also showed no further wave (not shown). We conclude that for water- (or electrolyte-) soluble thiol systems, a single sweep to sufficiently negative potentials is enough to regenerate the bare Au surface, ready for the next functionalization step by self-assembly of another organosulfur derivative.

This interpretation is confirmed by the simultaneous recording of the reflected laser intensity at a (constant) incident angle near the PSP resonance. The corresponding curve monitored during the voltage sweep of Figure 23(*a*) is given in Figure 23(*b*). For potentials from $U = -0.10$ V to $U = -0.86$ V, no change of the reflected intensity is seen, but simultaneous with the onset of the reduction current [cf. (*a*)] the decrease of the reflected light indicates the onset of the desorption of the SAM, which leads to a shift of the PSP resonance to lower angles and hence to a decrease of the reflected light if monitored at the low-angle slope of the resonance curve. As seen already in the cyclic voltammogram [refer to Figure 23(*a*)], the desorption proceeds in two steps, with the change in reflected intensity being qualitatively the integral over the cathodic wave. Upon cycling the potential back to $U = -0.10$ V, only a monotonous increase of the reflected intensity can be observed with a slope identical to the behavior of a bare Au substrate, which is given for reference in Figure 23(*c*). This change of the reflectivity of a bare Au/electrolyte interface has been observed before in electroreflectance studies and has been attributed to a change

←

Figure 22 (*a*) Interfacial architecture used in the kinetic mica waveguide experiment. A condensed monolayer of the phospholipid DPPE (compound 10; structural formula given in one of the *dashed boxes*) is transferred in a head-down configuration onto the freshly cleaved mica sheet. A second monolayer of DLPE (compound 8) doped with 5 mole% biotinylated DPPE (compound 9) is transferred onto this coated, hydrophobic substrate in the horizontal Langmuir-Schäfer technique. Injection of streptavidin leads to the formation of a protein monolayer by specific binding to the biotin "ligands." (*b*) Kinetic scan, i.e. recording of the change in reflectivity at a fixed angle of observation near a mica waveguide resonance as a function of time. (*c*) Same data as in (*b*), however, plotted as a function of $\sqrt{t}$. The diffusion constant of streptavidin in water can be derived from the *straight line*.

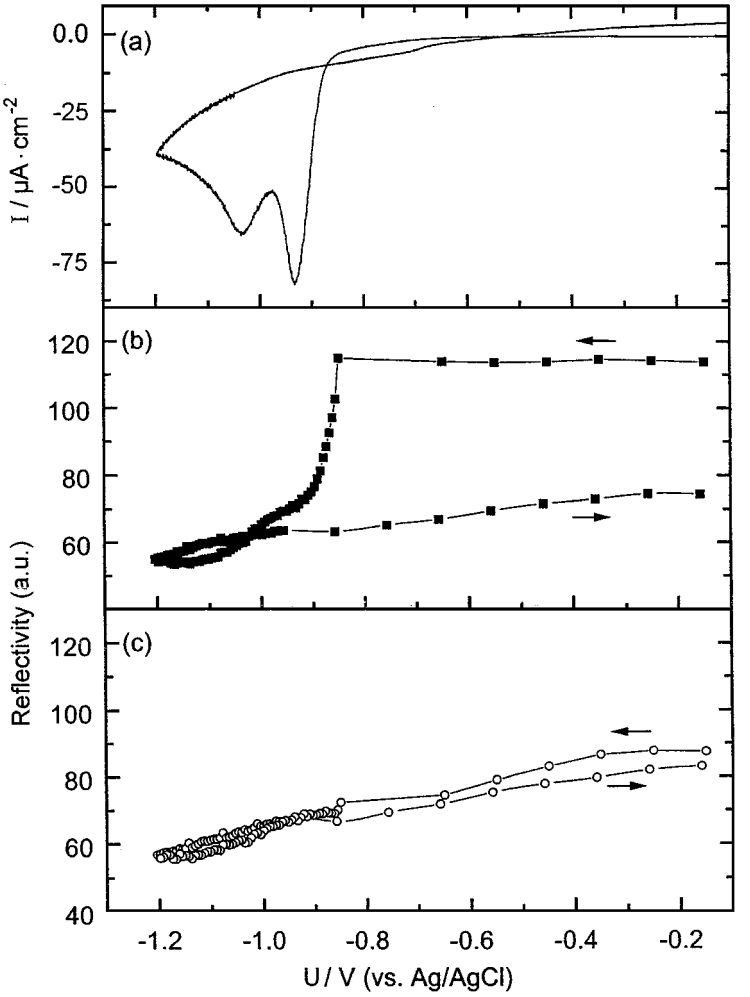

Figure 23 (*a*) Cyclic voltammogram taken in a conventional electrochemical cell [with a Pt wire as the counter electrode, Ag/AgCl as reference electrode, and the LaSFN9 high index glass/Au (50 nm)-substrate as the working electrode] integrated into a surface plasmon spectrometer (see Figure 18). The sample was a SAM of thiol (compound 6), adsorbed to the Au substrate for ≈1 h. Scan rate was 20 mV/s. The electrolyte solution contained 0.10 M KOH and was purged with N_2. (*b*) Kinetic reflectivity mode, i.e. recording of the reflected intensity at a fixed angle of observation while scanning the electrode potential [as in (*a*)], for a SAM of thiol (compound 6). (*c*) Same as (*b*), but for the bare Au substrate only.

of the optical constants of the topmost Au-layer at a thickness in the range of the Thomas-Fermi screening depth of the metal. The fact that this change is completely absent in the case of a SAM-coated Au surface might indicate that other effects originating from different surface processes contribute to this change in the optical properties of the unprotected, bare Au surface.

Another example for the use of the combination set-up surface plasmon optical/electrochemical spectrometer is summarized in Figure 24. Here, the fundamental concept for a controlled surface functionalization is based on the electropolymerization of a phenol derivative, carrying a covalently linked biologically active peptide (32). The employed synthetic linker peptide SLP1, corresponding to the amino acid sequence 1490–1507 of the cytosolic linker between domains III and IV of the rat cardiac sodium channel protein, was *N*-terminally modified with 3-hydroxyphenyl-acetic acid (HPA) using a spacer consisting of two lysine residues (HPA-KK-SLP1, compound 11) as shown in Figure 24(*a*).

Electropolymerization of HPA-KK-SLP1 at a gold surface was done by applying a cyclic potential known from cyclic voltammetry (CV) and was monitored by simultaneous SPR measurements. As the first step, the SPR cell was filled with HPA-KK-SLP1 (0.2 mg/ml in Sörensen buffer). During an equilibration time with no potential applied, strong adsorption of the peptide to the gold surface occurred [Figure 24(*b*)]. After 6 min, the cyclic potential was applied. After ten cycles (13 min), 70% of the layer had formed. Even after 60 min, the thickness of the layer still slightly increased and was determined to be 4.4 nm. The polyphenol layer was absolutely stable against repeated washing procedures with Sörensen buffer. The oscillations of the reflectivity following the potential oscillations are more-and-more damped out as the coverage of the bare electrode with a polyphenol layer proceeds. This is in qualitative agreement with the observation made with the thiol SAM-covered Au surface [see Figures 23(*b*) and (*c*)].

The course of the formation of the peptide layer was examined by recording the current as a function of the applied potential [Figure 24(*c*)]. In cycle 1, a small oxidation peak of the phenolic group is visible at $+0.6$ V, but no corresponding reduction peak, indicating an irreversible process. After the first few cycles, the current decreased significantly, as shown for cycles 11, 41, and 50. This indicates a rapid formation of the polyphenol layer with an almost complete surface coverage and a slow completion of the polymerization at the remaining defects.

In order to investigate receptor-ligand interactions, the peptide-functionalized gold electrode was incubated with polyclonal antibodies. To inhibit unspecific binding, free adhesion sites were blocked with 2% BSA/PBS. As shown in Figure 24(*d*), almost no adsorption of BSA occurred, proving a highly regular

(a)

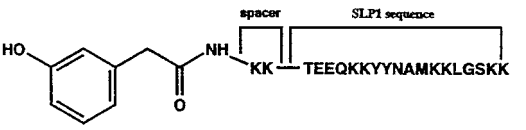
spacer
SLP1 sequence
HO
NH
KK
TEEQKKYYNAMKKLGSKK
O

11

(b)

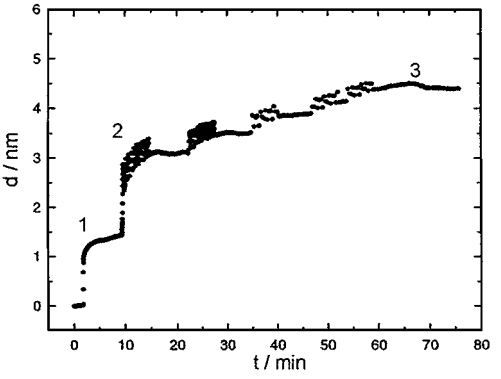
d / nm
t / min
1
2
3

(c)

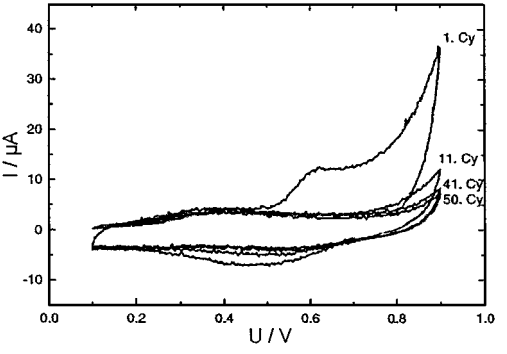
I / µA
U / V
1. Cy
11. Cy
41. Cy
50. Cy

(d)

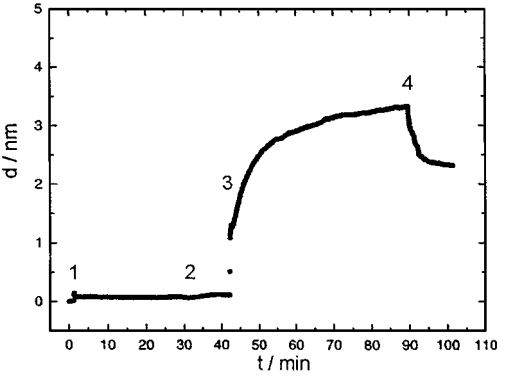
d / nm
t / min
1
2
3
4

polyphenol layer. After addition of the anti-SLP1 serum (50 μg/ml in PBS), a fast increase of the thickness of the layer within 10 min was observed. After rinsing, a total thickness of the specifically bound antibody was found to be 2.2 nm.

It is needless to say that this potential-controlled electropolymerization strategy for the functionalization of electrodes bears a particular potential for bio- and chemical sensor formats if used in combination with electrode arrays, the single elements of which can be coated individually!

Coupling by Grating Rotation

In this section, we demonstrate that the rotation of a grating structure with respect to the plane of incidence provides a new concept for the characterization of thin-film samples of different optical thicknesses (58). For a quantitative analysis, this scheme requires only a rotation of the sample at a fixed angle of incidence of the exciting laser beam. This facilitates the practical use of grating couplers.

A schematic of the set-up is shown in Figure 25. The gratings used in these studies were fabricated with a periodicity of $\Lambda = 0.5$ μm. The photoresist gratings were coated with about 200 nm Ag by evaporation in a vacuum chamber. Thin-film test coatings were prepared by depositing monomolecular layers of polyglutamate (see Figure 12) by the Langmuir-Blodgett-Kuhn (LBK) technique. The mounted gratings could be rotated by an angle ψ with respect to the plane of incidence defined by the incident (angle of incidence θ with respect to the sample normal) and the reflected laser beam. At $\psi = 0$, the grating vector $G = 2\pi/\Lambda$ was parallel to the photon wavevector projection $k_x^{photon} = k^{photon} \sin\theta$.

Figure 26 summarizes a series of angular scans (reflectivity R vs angle of incidence θ) taken at various rotation angles ψ as indicated. Two sets of data are shown: the first was taken for the bare Ag grating. In order to compensate for the increasing angular mismatch between the grating vector G and the direction

←

Figure 24 (*a*) Polymerizable synthetic peptide derivative HPA-KK-SLP1 (compound 11). The SLP1-peptide represents the sequence 1490–1507 of the cytosolic linker between domains III and IV of the rat cardiac sodium channel protein. (*b*) SPR kinetics of the physisorption and the electropolymerization of compound 11 on a gold substrate. Five sets of ten electropolymerization cycles each with a hold of 7 min between the sets are applied. *1.* physisorption of the functionalized phenol; *2.* polyphenol layer formation using electropolymerization; *3.* extensive rinsing with buffer. (*c*) Cyclic voltammograms of the electropolymerization of HPA-KK-SLP1 (0.2 mg/ml in Sörensen buffer) at a gold substrate versus Ag/AgCl. The sweep rate was 50 mV/s. Cycles 1, 11, 41, and 50 are shown. (*d*) SPR kinetics of the binding of the anti-SLP1 serum to the electropolymerized polyphenolpeptide-layer on a gold substrate. *1.* Blocking of unspecific adhesion sites with 2% BSA/PBS; *2.* Washing with PBS buffer; *3.* Incubation with antibody (50 μg/ml in PBS); *4.* Washing with PBS buffer.

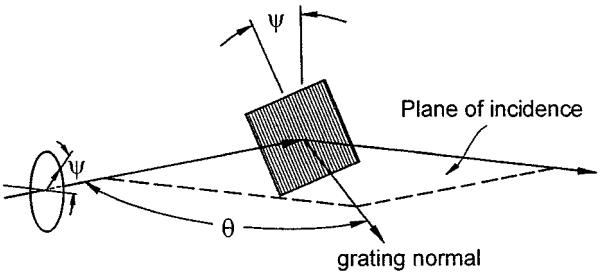

Figure 25 Schematic of the experimental construct for surface plasmon optics with rotating grating couplers. The plane of incidence is defined by the incoming (angle of incidence θ) and the reflected laser beam. The grating can be rotated around an axis parallel to its normal by ψ. The polarization of the linearly polarized laser beam can follow this rotation.

of the initially p- (i.e. linearly in the plane of incidence) polarized light, the polarizer in the exciting laser beam was also rotated for each θ-scan by ψ. This way, all resonance curves are nearly equally deep. At a certain cut-off angle, ψ_0, no PSP excitation at any angle θ can be found. If the grating was coated by four layers of PG, the expected angular shift of the PSP resonance curve was observed. For $\psi = 0$, this finding corresponds to the usual PSP spectroscopical mode for the evaluation of the optical thickness within the Fresnel theory for ultrathin organic coatings. Considering that we are concerned with a grating constant of $\Lambda = 0.5\ \mu$m, we are operating in the second Brillouin zone where any thin-film coating shifts the PSP resonance to smaller angles θ (see Figure 6). With increasing rotational angle ψ, this angular θ-shift relative to the bare Ag curves increases. As a result, the LBK coating allows for PSP excitation even at angles ψ that are already beyond the cut-off value ψ_0 for the bare Ag. But also in the coated areas, eventually the characteristic cut-off angle, ψ_1, is reached.

This PSP resonance behavior can be understood on the basis of the momentum-matching scheme given in Figure 27. Shown are quarter circles with radii corresponding to the grating vector $|G|$, and the PSP wavevectors $|k_{sp}^{Ag}|$ and $|k_{sp}^{Ag+4PG}|$, respectively. Now, for a given sample rotation ψ, the grating vector G corresponds to the arrow from the origin to the respective circle. The photon wavevector projection as obtained from the corresponding reflectivity scan adds vectorially parallel to the x-direction which is defined by the geometry of the reflectivity measurement. All thus determined values for the resonance momentum matching conditions, indeed, fit the respective PSP wavevector circles. This picture also explains the different cut-off angles ψ_i. Beyond these, the addition of the photon wavevector projection does not reach a point on the respective PSP-circles.

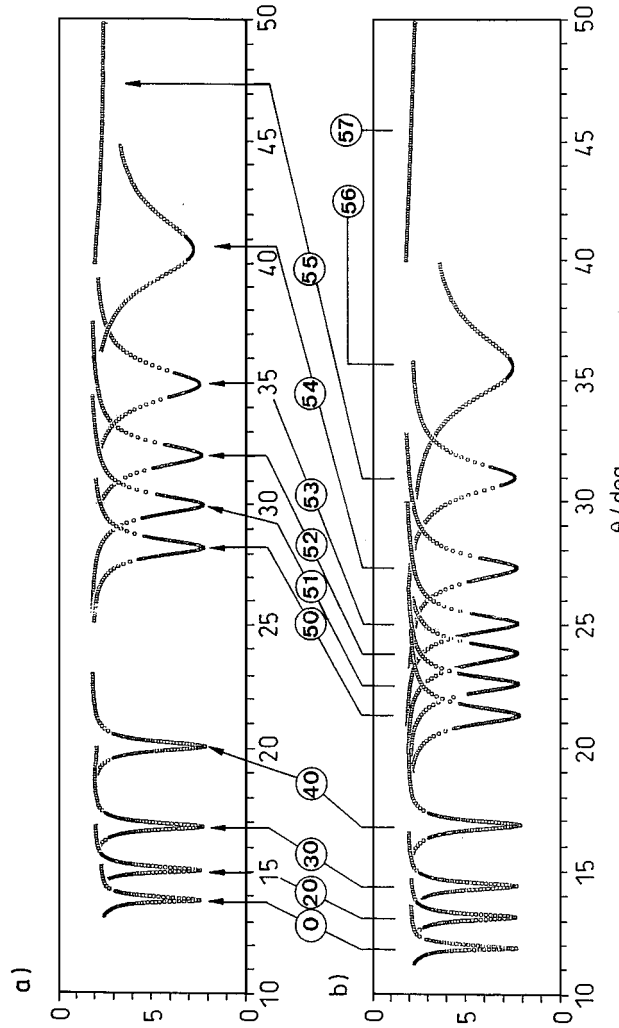

Figure 26 Series of angular θ-scans of the reflected intensity (*a*) for a bare Ag-grating, and (*b*) after deposition of four layers of polyglutamate at various sample rotations ψ, as indicated. Note the shift of the PSP-resonance to higher θ-values with increasing ψ.

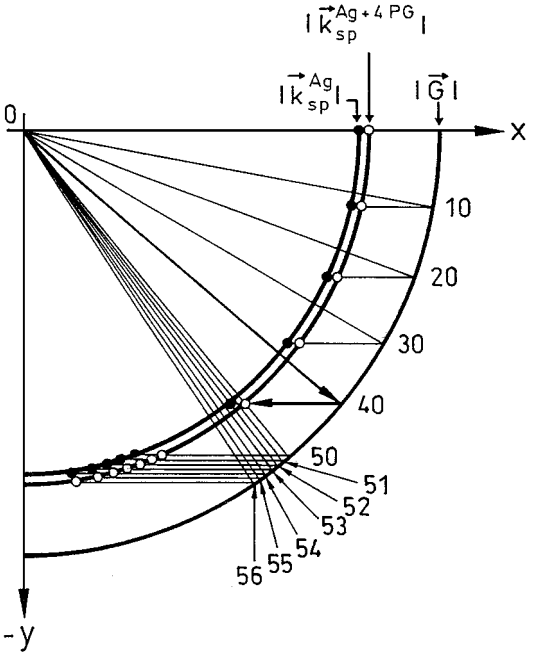

Figure 27 Momentum-matching scheme for the PSP excitation experiments presented in Figure 26. *Quarter circles*, the grating vector $|G|$, and the PSP wavevectors, $|k_{sp}^{Ag}|$ and $|k_{sp}^{Ag+4PG}|$, respectively. By rotation of the grating by ψ and the vector-addition of the photon wavevector projection k_{ph}^{x} (parallel to the x-axis), a point on the surface plasmon wavevector circle can be reached that leads to the resonant excitation of PSP waves. Above a certain cut-off angle ψ_c, this is no longer possible.

This non-collinear momentum addition between the projection of the photon wavevector $\vec{k}_{ph}^{x}$, the grating vector $\vec{G}$, and the momentum of the launched mode with $\vec{k}_{sp}$, can be visualized directly if, instead of a surface plasmon with a propagation length of only a few tens of μm, a waveguide mode is excited in an all-dielectric configuration, i.e. with a propagation of a few mm to cm (see Figure 10). The scattering losses of such a GOW can be monitored and used to quantify its propagation direction (59). An example is given in Figure 28. Figure 28(*a*) gives a photograph of the structure, Figure 28(*b*) gives a schematic of the situation. The sample was a polystyrene slab waveguide of $d \approx 1$ μm thickness prepared by spin-coating onto a glass substrate that contained two grating structures each with a grating constant of $\Lambda = 1000$ nm fabricated by reactive ion etching. Grating G_1 was used to couple the exciting photon, propagating along the x-direction via the grating vector $\vec{G}$, to a waveguide mode propagating with $\vec{k}_{GOW}$ along a direction rotated relative to the x-direction by the

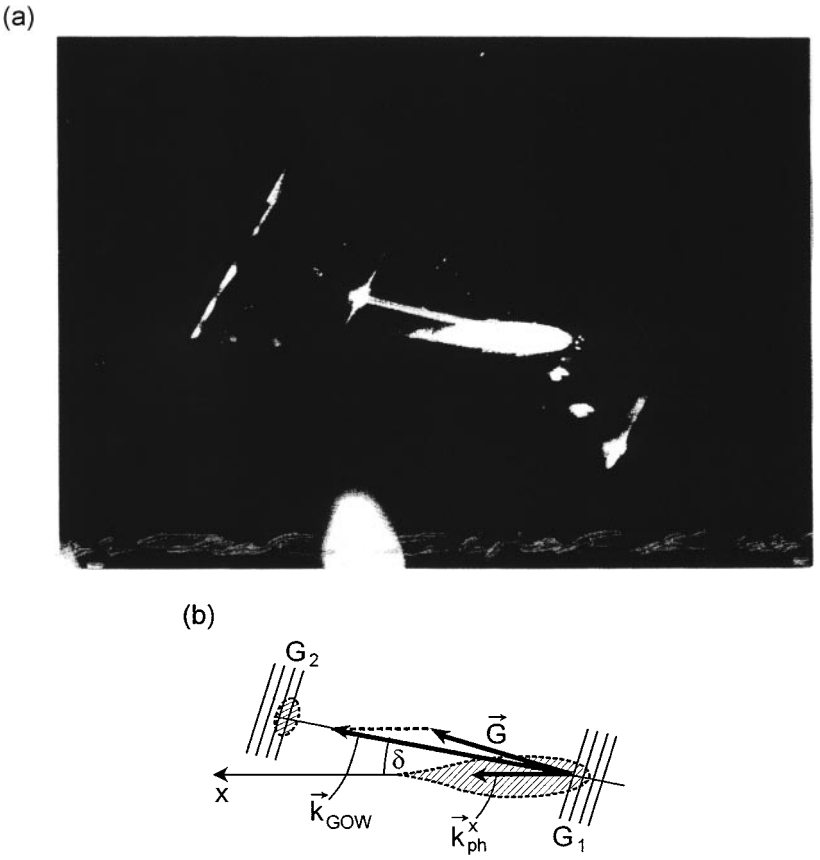

Figure 28 (*a*) Photograph of the coupling geometry with the coupling spot and a streak of the guided light. (*b*) Sketch of the coupling geometry and the direction of the various wavevectors: The grating G_1 couples the photon wavevector projection k^x_{ph} to the waveguide momentum k_{GOW} by means of the grating vector $\vec{G}$. δ denotes the deflection angle between the x-direction represented by the incident beam and the propagating mode.

angle δ. The photograph in Figure 28, hence, gives direct evidence for the vectorial addition principle of the momenta of photon wavevector and grating vector.

If we plot the reflected intensity at a fixed angle θ (taken from the angular scans in Figure 26) as a function of the various ψ-values, we see the striking difference between bare Ag and the polymer-coated sample: The θ-contrast of the "classical" PSP-resonance spectroscopy is converted into a ψ-contrast at a fixed angle of incidence. This is documented in Figure 29 for the reflectivity data taken at $\theta = 35^\circ$. The ψ-resonance curves are about as narrow as the θ-scans with a comparable shift induced by the LBK layer.

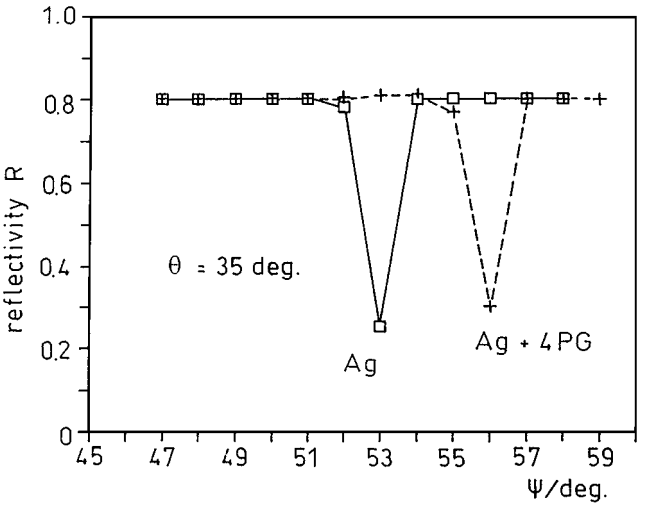

Figure 29 Plot of the reflected intensities at a fixed angle of incidence, $\theta = 35°$, as derived from θ-scans at fixed angles of rotation ψ. The different angular positions for the PSP resonance in bare Ag-gratings (-□-) and after deposition of four PG LBK-layers (- + -) is the basis for the ψ-contrast.

Integrated Mach-Zehnder Interferometer

As we pointed out above, the planar waveguide layer is a structure that is able to guide light through its confinement in just one dimension, i.e. normal to the layer. If a second confinement is introduced, a channel waveguide or optical fiber is obtained where the light now propagates in a "pipe," confined to the cross-section of the high-index core surrounded by lower index cladding material. As far as channel waveguides are concerned their technological importance originates from visions of an opto-board that allows for (optical) data processing with the speed of light.

We demonstrated already that the evanescent tail of a guided optical mode that reaches out into the surrounding dielectric medium can be employed to characterize thin-(additional) organic coatings in an approach equivalent to the use of surface plasmon optics (refer to Figure 22). The same considerations also apply to channel waveguides owing to their evanescent reach-out into the surrounding material. We demonstrate this in the following for a very special channel waveguide format, i.e. the integrated Mach-Zehnder interferometer (iMZI).

In all the examples discussed so far, the deposition of a thin film coating of higher refractive index than the environment resulted in a momentum increase of the guided mode (surface plasmons as well as guided optical waves). This was compensated for (and thereby detected) by increasing the projection of

the photon wavevector of the exciting photon, i.e. by increasing the angle of incidence to retune into resonance, or by rotating the grating in the case of a non-collinear grating coupling scheme. For the guided mode itself, an increase in its momentum is the result of the overall increase of the effective refractive index of the interfacial materials probed by the bound wave. This is equivalent to a decrease in its phase velocity. After a given propagation distance, therefore, the phase of this wave is changed relative to an unmodified guided mode, and the coherent interference pattern of the combined waves changes in a characteristic way.

In the iMZI-format schematically depicted in Figure 30(*a*), the output power P measured at (S) after the recombination of the light guided through channel 1 and 2, respectively, depends on this phase change $\Delta\phi$, according to:

$$P = \frac{P_0}{2}(1 + \cos\phi), \tag{36.}$$

with P_0 being the light power coupled into the device (ignoring propagation losses owing to absorption or scattering).

The phase change that a mode experiences propagating a distance, L_{sens} [refer to Figure 30(*a*)], has two contributions:

1. It depends on bulk refractive index changes Δn_d, of the surrounding medium, e.g. the solution with the analyte, to the extent that it is probed by the evanescent tail of the guided mode; and 2. it varies as a thin film is deposited onto the guiding layer. Both effects result in a phase change given by (60):

$$\Delta\phi = L_{sens} \cdot \frac{2\pi}{\lambda}\left(\frac{\partial N}{\partial n_d}\Delta n_d + \frac{\partial N}{\partial d_{layer}} \cdot \Delta d_{layer}\right), \tag{37.}$$

with λ being the wavelength of the light, N the effective refractive index of the structure describing the propagation behavior of the guided mode, and $\frac{\partial N}{\partial n_d}$ and $\frac{\partial N}{\partial d_{layer}}$ depending on optical channel parameters like cross-section and refractive indices.

Some characteristic features and dimensions of the iMZI employed in our studies (61) are summarized in Figure 30. The two branches of the iMZI had an effective length $L_{sens} = 12$ mm. The SiO_2 buffer layer [Figure 30(*b*)] on top of the Si substrate had a thickness of $\approx$2.5 μm. The active guiding structure was made from siliconoxynitride with a layer thickness of $d = 350$ nm and a refractive index of $n = 1.55$. Optical beam confinement was achieved by etching a rib into this layer, 2 μm wide and $\approx$55 nm in height. In order to preclude unwanted environmental influences, the whole chip was covered with 2 μm SiO_2. The position of the liquid microcell was defined by reactive ion etching a window into the SiO_2 cover [Figure 30(*b*)]. The structure was completed by pressing a PMMA cover slip to the chip with a parafilm mask (500 μm thick) as seal in between. This mask was structured such as to define two separate

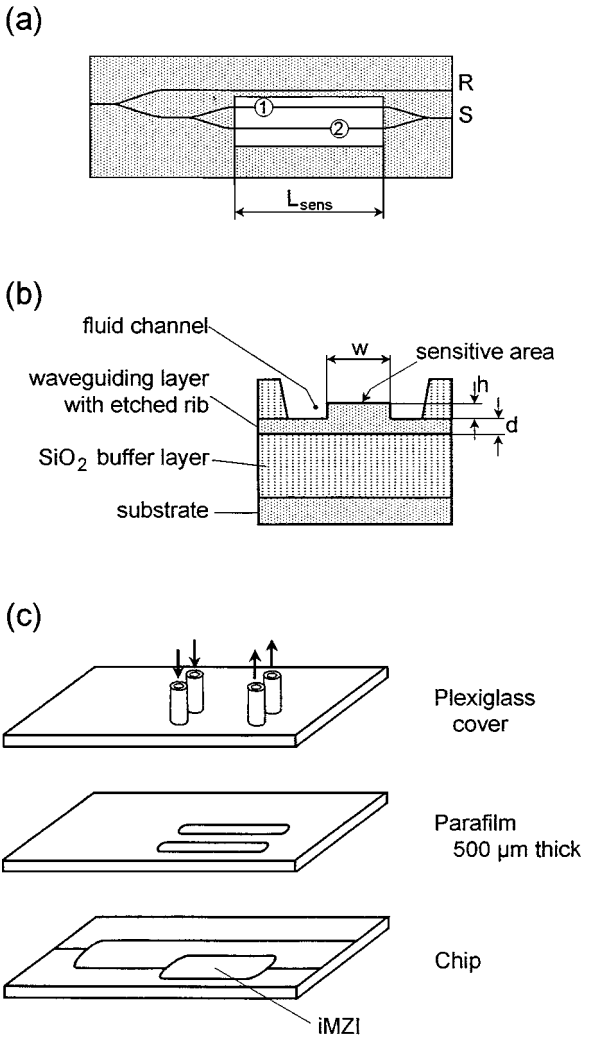

Figure 30 (*a*) Waveguide chip assembly with integrated Mach-Zehnder Interferometer. *R*, reference channel waveguide; *S*, signal output of the two interfering channels 1 and 2. (*b*) Cross-section of the guiding structure with integrated fluid channel. (*c*) Schematic of the final assembly, consisting of the chip, a parafilm seal with two separate fluid channels, and a Plexiglas cover with separate inlet and outlet for the two microcuvette channels. (*d*) Structural formula of the two end-functionalized silane-derivatives used in the assembly of a binary mixed SAM. Silane compound (compound 12) carries the biotin group; compound 13 is a COOH-terminated diluent molecule. (*e*) Specific binding of streptavidin to the biotin-functionalized silane-SAM on the waveguide structure. The output signal [monitored at *S*, cf. (*a*)] is given after the injection of a 10^{-6} M streptavidin solution (in 0.5 M NaCl) to the 1st channel only, resulting in a 6π phase shift.

(d)

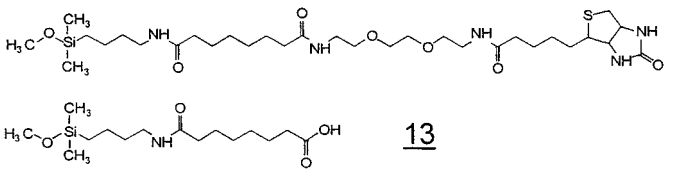

(e)

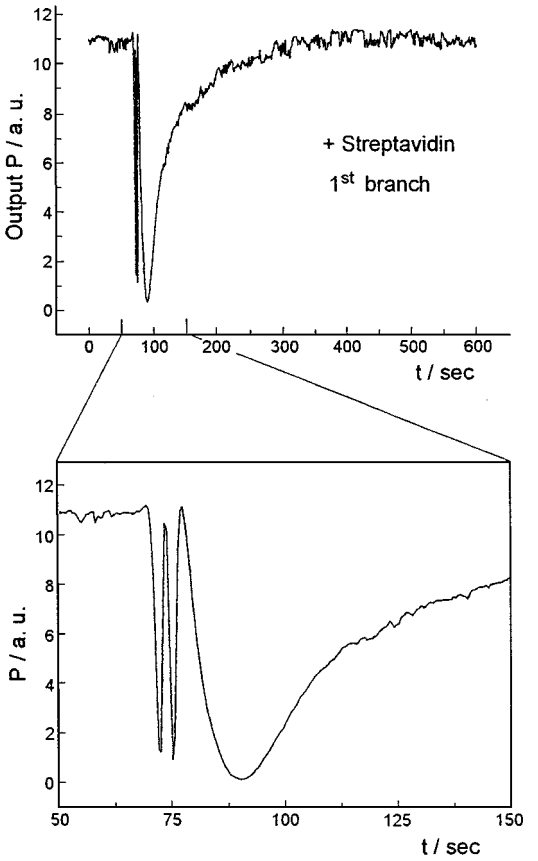

Figure 30 (*Continued*)

channels for the liquid flow [Figure 30(*c*)]. Four holes in the Plexiglas cover allowed then for the individual perfusion of the liquid channels in contact with the two branches of the iMZI (62). The TE-polarized chopped light of a 5 mW HeNe laser ($\lambda = 632.8$ nm) was endfire-coupled to the interferometer, and the out-coupled light monitored with lock-in-technique.

As a model reaction we again choose to study the binding of streptavidin. As in the other studies with the biotin/streptavidin system, a self-assembly strategy was chosen. Long-chain derivatives of dimethyl-monomethoxy-silanes, carrying as a functional endgroup either the biotin group [compound 12 in Figure 30(*d*)] or a COOH-moiety [compound 13 in Figure 30(*d*)] were coadsorbed from binary solutions. The binding capacity of the mixed monolayers towards streptavidin molecules were first characterized by surface plasmon spectroscopy. For this purpose, the Ag substrates used for the reflectivity measurements in the Kretschmann configuration were precoated by evaporating SiO_x, thus mimicking the glassy surface of the iMZI. We found a thickness increase by 2.8 nm upon injection of a streptavidin solution and binding of the protein to the functionalized silane-SAM.

If the equivalent experiment is performed with the iMZI, one can see from Figure 30(*e*) that the injection of a 10^{-6} M streptavidin solution (in 0.5 M NaCl) into the first liquid channel causes an intensity modulation corresponding to about 6π. Injection of the identical streptavidin solution into the second channel reverses the oscillations and even overcompensates the phase shift of the first branch by π (not shown).

Obviously, the concept of introducing a selective surface functionality for specific biorecognition and binding by the co-assembling of correspondingly end-functionalized silane molecules developed for large-area planar substrates proved also to be ideally suited for the modification of the channel waveguide surfaces for biosensing purposes with the iMZI. These binary mixed SAMs provide an interfacial architecture that can be optimized for specific binding reactions while simultaneously suppressing nonspecific binding.

The sensitivity of a given channel waveguide for small thickness variations induced by a binding reaction to its surface is determined by $\frac{\partial N}{\partial d_{layer}}$ (see Equation 37). Inserting the approximation given for planar waveguides (60) into Equation 37, one obtains a theoretical sensitivity of the iMZI for monitoring biorecognition reactions of $\Delta\phi/\Delta d_{layer} = 2.9\pi/\text{nm}$ for $n_{layer} = 1.45$. The experimentally determined phase change upon binding of (a monolayer of) streptavidin to the biotin-sites on the channel, $\Delta\phi \approx 6\pi$, compares well to this expectation if we assume the formation of a protein monolayer of 2.8 nm thickness, as in the case of the SPS experiment. Accepting a lower bound for the unambiguous monitoring of binding events of $\Delta\phi \approx \pi/20$, one thus calculates an experimentally determined lower limit of the sensitivity of the device of

about 1/100 of a streptavidin monolayer, corresponding to $\Delta d_{min} = 0.02$ nm, equivalent to a mass coverage of about 2 ng/cm^2. This sensitivity is at least one order of magnitude better than is obtainable with surface plasmon spectroscopy. One has to keep in mind, however, that this is possible only because of the relatively long sensing path, integrating all the subtle phase changes of the propagating mode. The propagation ($\hat{=}$ integration) length in a typical SPS experiment is in the order of a few tens of μm only, and could be further reduced to the few μm range (e.g. by using Au substrates and operating further in the blue spectral range). L_x, on the other hand, determines the minimum spot size of a highly integrated multielement detector array operated in a surface plasmon microscopic mode for massive parallel (bio-) sensing (63). In other words, one can either optimize the sensitivity (the contrast) or the lateral resolution, but never both at the same time!

Monitoring Refractive Index Changes

In the preceding sections, we were concerned—in one way or another—with thickness changes of a thin coating which could be monitored in various sample formats by surface plasmon or guided optical wave spectroscopy. In this section we describe a few examples where a thin film, once prepared, changes its optical properties under the influence of an external parameter, which can be either heat, pressure, light, or an electric field. In the case of surface plasmon optical measurements with ultrathin coatings one has to consider, of course, whether these modifications also result in a thickness change that might require additional data from, for example, X-ray reflectometry measurements. For films that can be investigated by waveguide spectroscopy, the refractive index as well as the geometrical thickness (and their modifications) can be determined independently, as has been pointed out already.

The following temperature-dependent recording of waveguide spectra performed with PMMA films prepared by spin-coating are an example of this. Shown in Figure 31 are the two modes found in p-polarization [Figure 31(*a*)] or s-polarization [Figure 31(*b*)] for a film of $\approx$520 nm thickness. Their respective angular positions depend in both cases significantly on the temperature: The full curves were taken at $T = 70^\circ$C, the broken ones at $T = 150^\circ$C.

For each temperature, the quantitative analysis within a Fresnel matrix formalism indicates that, indeed, these films can be described by their temperature-dependent thickness, d, and their temperature-dependent yet isotropic refractive indexes, n. For the film of Figure 31(*a*) and (*b*), we obtain $n = 1.483$ and $d = 518$ nm at $T = 70^\circ$C; and $n = 1.474$ and $d = 527$ nm at $T = 150^\circ$C. The corresponding data obtained at intermediate temperatures for another sample are given in Figure 31(*c*). Over the temperature range investigated, i.e. between 50°C and 160°C, the film thickness increases from $d = 560$ nm to

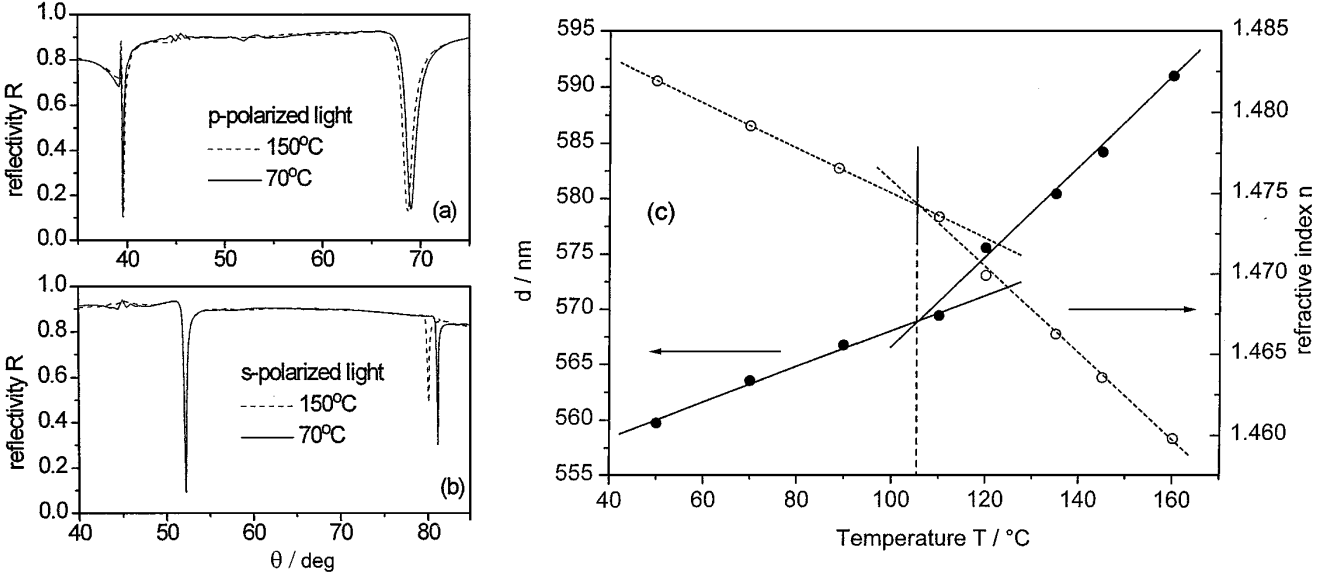

Figure 31 Angular reflectivity curves (R-vs-θ) obtained for a spin-cast PMMA film (*a*) with p-polarized and (*b*) with s-polarized light of a HeNe-laser at two different temperatures: *full curves* were taken at $T = 70°\text{C}$, *broken curves* at $T = 150°\text{C}$. From the Fresnel fits (not shown), the temperature dependence of the thickness d and the (isotropic) refractive index n are obtained. (*c*) Thicknesses (-●-) and refractive index values (-o-) of a PMMA film as a function of temperature. The data were obtained from Fresnel fits of waveguide spectra like the ones displayed in (*a*) and (*b*). From the slopes of the linearized temperature dependence of $d(T)$ and $n(T)$, one obtains the coefficients $\kappa = \partial n/\partial T$ and $\beta = \frac{1}{d} \cdot \frac{\partial d}{\partial T}$.

$d = 590$ nm, whereas its refractive index decreases from $n = 1.485$ to $n = 1.460$. The temperature variation of both values seems to follow two linear regimes, with a break at $T \approx 107°C$, which is identified as the film's glass transition temperature, T_g. The two parameters, $\kappa = \partial n/\partial T$ and $\beta = \partial d/\partial T \cdot (1/d)$, which describe the temperature variation of the refractive index and the (one-dimensional) thermal expansivity, respectively, can be obtained from the linear slopes below and above T_g.

If a temperature increase results in the expansion of the film and a corresponding decrease of its refractive index, a pressure increase should have the counteracting effect. In order to study this fundamental phenomenon, we constructed a thermostated pressure cell for pressures up to $2000 \cdot 10^5$ Pa that can be implemented into a surface plasmon/waveguide spectrometer. A cross section (with all parts to scale) of the cell is presented in Figure 32. The main body is

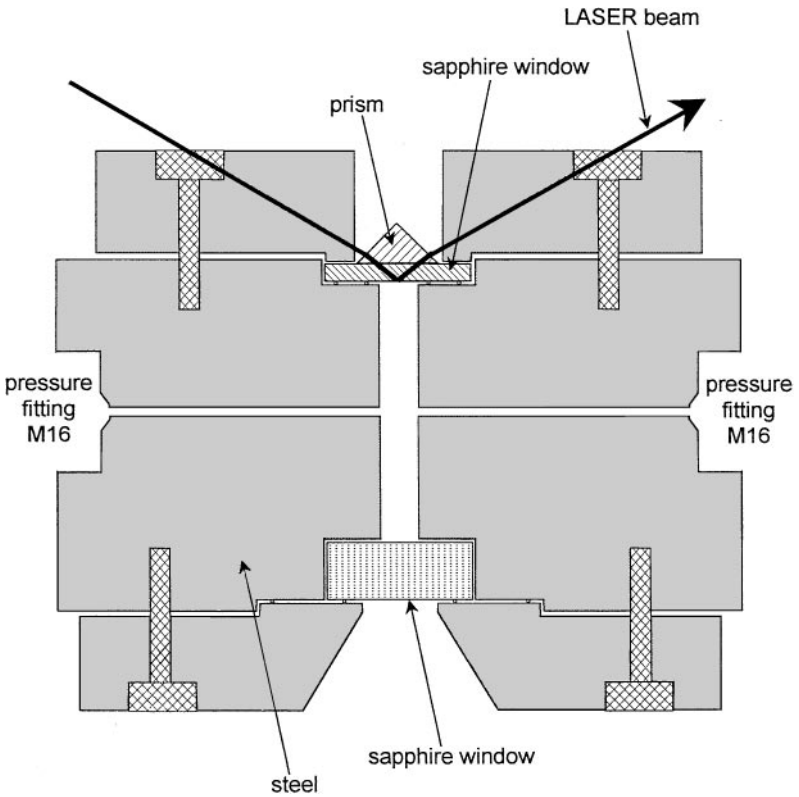

Figure 32 Schematic of the high pressure cell used for the surface plasmon and optical waveguide spectroscopy under pressure up to $2000 \cdot 10^5$ Pa.

made from stainless steel and the two sapphire windows are sealed by Au-wires. A prism can be index-matched to the thinner window, and a narrow cut in the top cover of the high pressure cell allows one to couple laser light by means of the prism to the Au- or Ag-coated inner surface of the sapphire window. Prior to final mounting, the latter can be coated with the thin film sample of interest—in our case a thin PMMA film of about 2 μm thickness, prepared by spin-coating. As the pressure medium, one can use any liquid (such as H_2O, methanol, ethanol, or supercritical CO_2) that is inert with respect to the sample.

For the experiment presented in Figure 33, we used H_2O as the pressure medium, knowing that a slight interaction with the PMMA coating could occur. Within the accessible angular range ($45^\circ < \theta < 67^\circ$) four modes in p-polarization as well as the critical angle for total internal reflection could be observed. For better clarity, the plot in Figure 33(*a*) presents only data recorded between $\theta = 47^\circ$ and $\theta = 61^\circ$ at room temperature ($T = 25^\circ$C), and at increasing pressures of 15, 200, 400, 600, 800, and $1000 \cdot 10^5$ Pa, respectively.

Two effects are superimposed: the change in the optical density of the pressure medium and that of the film. The former manifests itself in the pressure-shift of the critical angle, θ_c. If observed with an uncoated bare sapphire slide/prism set-up, it can be very accurately determined [refer to Figure 1(*b*)] and used to quantitatively describe the pressure dependence of the refractive index of the liquid medium in the pressure cell. The data for H_2O are given in Figure 33(*b*). The experimental points can be well described by a theoretical curve calculated by the Lorentz-Lorenz treatment. The shift of θ_c in Figure 33(*a*) originates from this effect. It can be quantitatively subtracted from the pressure-effect on the waveguide resonances, which then can be used to evaluate the variation of the refractive index and the thickness of the PMMA film at different pressure. The results are given in Figure 33(*c*) for the index and in (*d*) for the thickness. A linearized description of the pressure effect on the film's properties would not fit the data at higher pressures, but Tait's model [*full lines*, Figure 33(*c*) and (*d*)] gives a satisfying agreement (64, 65).

Another major area of research related to thin films concerns the materials, physics, and chemistry of photoreactive systems. Numerous schemes have been

Figure 33 (*a*) Series of reflectivity scans taken with a PMMA film of $d = 2.2$ μm thickness at increasing pressure ($p = 15, 200, 400, 600, 800, 1000 \cdot 10^5$ Pa). Note the shift of the critical angle caused by the pressure-dependent refractive index of the transducer medium, water, as well as the shift of the waveguide mode. (*b*) Pressure-dependence of the refractive index of water at $T = 25^\circ$C, as obtained from the shift of the critical angle for total internal reflection [cf. (*a*)]. The full curve is a Lorentz-Lorenz fit to the experimental data points. (*c*) Pressure-dependent refractive index; and (*d*) pressure-dependent thickness of a PMMA film characterized by waveguide spectroscopy. *Full curves*, theoretical predictions based on Tait's model (64).

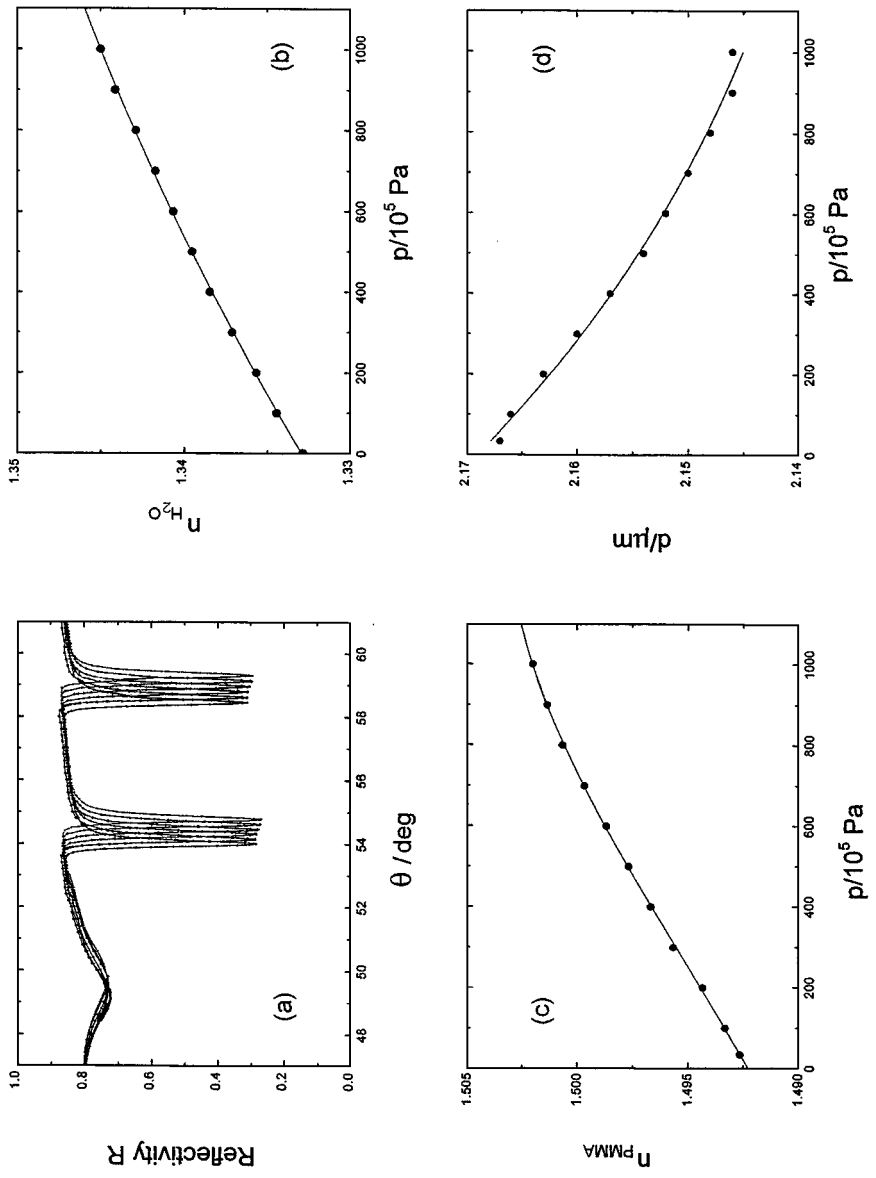
Reflectivity R
θ / deg
(a)
n_{H_2O}
p/10^5 Pa
(b)
n_{PMMA}
p/10^5 Pa
(c)
d/μm
p/10^5 Pa
(d)

proposed and chemically realized regarding how a beam of pump light of one wavelength, polarization, power density, and the like can modify a material in such a way that a second (probe) light beam experiences a different interaction with the material, resulting in the idea of manipulating light by light, an essential element for all data processing and storing concepts of modern photonics.

An important role in this context is the phenomena associated with the well-established *trans* ↔ *cis* photoisomerization of azobenzene derivatives (42). We already introduced in Figure 13 one example in which such a chromophore was coupled to a silane group, thus allowing for the self-assembling of these molecules to form a highly organized monomolecular coating of only 0.9 nm thickness atop a glassy substrate. The questions remain whether such an assembly allows for the isomerization process and whether this can be monitored by surface-sensitive optical techniques.

If the monolayer of the azosilane is assembled in the dark-adapted *trans* form of the azobenzene, the illumination with UV light of $\lambda = 360$ nm might result in the isomerization to the *cis* form; the associated optical thickness reduction that we anticipate, however, is too small to be detected as an appreciable shift of the PSP resonance curve (see Figure 13).

If this change in optical thickness is followed on-line (during irradiation) by recording the reflected intensity at a fixed angle of incidence [e.g. $\theta = 45^\circ$; refer to Figure 13(*b*)] a kinetic analysis of the optical thickness change can give information about the reaction rates, the equilibrium changes, the reversibility, and so on. The latter important aspect is shown in Figure 34. One should emphasize that this optical switching is observed for a 0.9 nm ultrathin monomolecular layer. The first rapid decrease of the reflectivity upon UV irradiation can be restored by switching to visible light (450 nm), which isomerizes the azobenzenes back into the *trans* form. These reaction cycles can be conducted many times. It is important to note that, given the signal-to-noise level of these data, index changes smaller than $\Delta n = 0.001$ can be monitored in thin layers that are only 0.9 nm thick.

Once again, the full potential of waveguide spectroscopy becomes evident for the next example of a photoreactive thin film system. The sample was prepared by the LBK technique from monolayers of the azobenzene-functionalized polyglutamate P2,10 (compound 14). Its structural formula is given in Figure 35(*a*). 156 monolayers were assembled into a waveguide structure of $d = 0.37$ μm to allow for the excitation of one s- and one p-polarized waveguide mode. The angular scan as obtained for the dark-adapted *trans* state of the chromophore with p-polarization is given in Figure 35(*b*), labeled *dark/Blue*.

Upon irradiation with unpolarized UV light $\lambda = (360 \pm 30)$ nm, *trans* → *cis* photoisomerization takes place, and the mode shifts its angular position to lower incidence angles [labeled *UV* in Figure 35(*b*)]. The mode recovers exactly

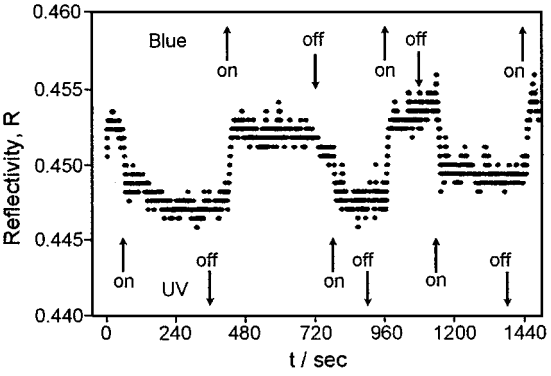

Figure 34 Optical thickness change as obtained by recording the reflected intensity of the azosilane sample of Figure 13 at a fixed angle of incidence [$\theta = 45^\circ$; refer to Figure 13(*b*)] while irradiating. The moments of turning the irradiation light on and off are indicated by *arrows*.

its initial angular position after blue light (450 $\pm$ 30) nm irradiation, with the subsequent *cis* $\rightarrow$ *trans* back-photoreaction [see Figure 35(*b*)]. The angular reflectivity scans for both TM and TE light were taken in the dark, i.e. with the pump beam off, and with the waveguide modes propagating successively parallel and perpendicular to the dipping direction of the LBK preparation by rotating the sample. For each switching step, the irradiating light (UV and blue) was kept onto the sample for 12 min to reach the photostationary state of the photoisomerization reaction. After the UV light irradiation, the angular positions of the guided modes remain unchanged during the reflectivity scan (in the dark), because the *cis* $\rightarrow$ *trans* thermal back-reaction needs more than 15 h to be completed at room temperature, and the *cis* state could be considered to be stable within the time scale of minutes (66).

An example of the experimental realization of the principle of switching light by light is given in Figure 35(*c*). The reflected intensity is plotted as it is recorded at a fixed angle of incidence [$\theta_{obs} = 40^\circ$; see Figure 35(*b*)] as a function of time. Upon irradiating the sample with UV light [*arrow* labeled UV in Figure 35(*c*)] the induced shift of the TM mode to lower resonance angles causes the high reflectivity to decrease from $R = 0.83$ to $R = 0.10$ within a few minutes. Switching to blue irradiation light [*arrow* labeled Blue in Figure 35(*c*)] results in a fully reversible restoration of the high reflectivity. These photoinduced switching cycles can be repeated many times without fatigue.

From all measurements (with p-polarized light and with s-polarization, with $k_{GOW} \perp$ dipping and $\parallel$ dipping direction), one can calculate the evolution of in-plane (n_x, n_y) and out-of-plane (n_z) refractive indices of the P2,10 LBK structure, under successive UV and blue unpolarized light irradiation cycles

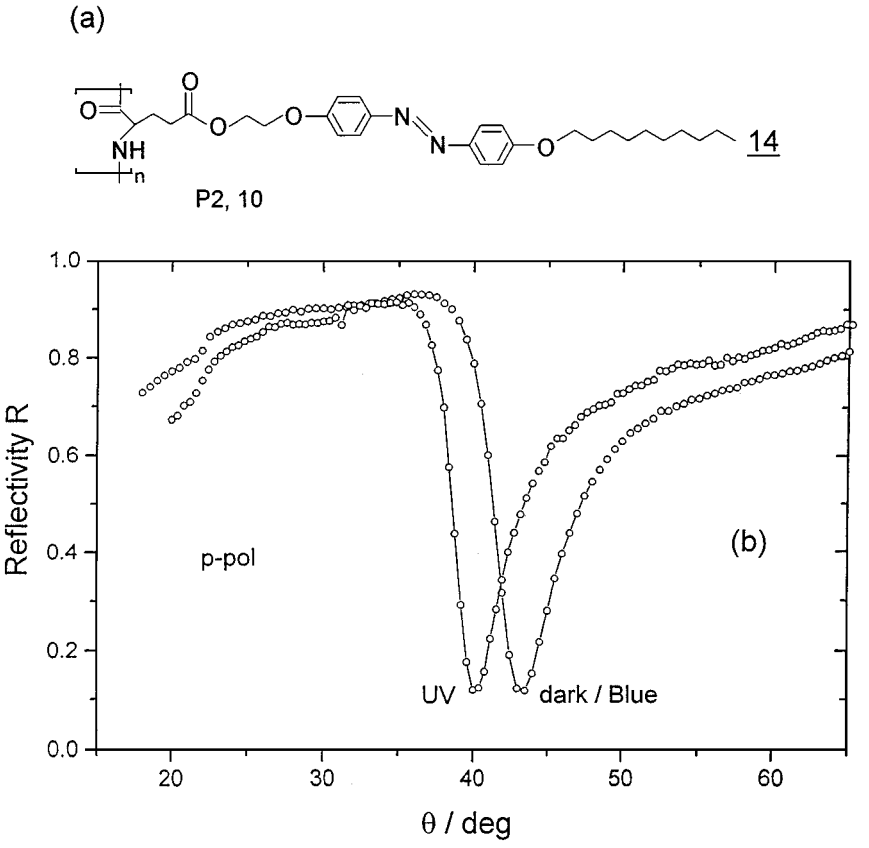

Figure 35 (*a*) Structural formula of an azobenzene-functionalized polyglutatmate, $P_{2,10}$ (compound 14). (*b*) TM light (p-polarized) mode spectra guided into the LBK polymer film consisting of 156 $P_{2,10}$ monolayers. *Dark*, *UV*, *Blue*: angular position of the mode before any irradiation, after a 360-nm UV light irradiation, and after 450-nm blue light irradiation, respectively. (*c*) Time evolution of *trans* $\leftrightarrow$ *cis* photoisomerization-induced back-and-forth switching in LBK structures of $P_{2,10}$ films consisting of 156 monolayers. These transients have been recorded by using WGS and by setting the goniometer at a fixed angle corresponding to the resonance condition while irradiating with UV or blue light. The moments for turning the photoactive light (UV or blue) on and off are indicated by *arrows*. (*d*) Evolution of the indices of refraction in the plane of the LBK ($P_{2,10}$; 156 monolayers) structure (n_x, n_y), and in the perpendicular direction (n_z) under different conditions. The first column refers to the sample before any irradiation (*New*); columns *UV, blue*, the sample after UV (360 nm) and blue-light (450 nm) irradiations, respectively. The high anisotropy shown in columns *New* and *blue* indicates a highly optically anisotropic LBK structure. *UV* shows a much less optically anisotropic structure. The evolution of the mean refractive index *n* under successive UV and blue-light irradiations suggests that the azo-molecules are switched between the two conformations (e.g. *cis* and *trans*) without a photobleaching effect.

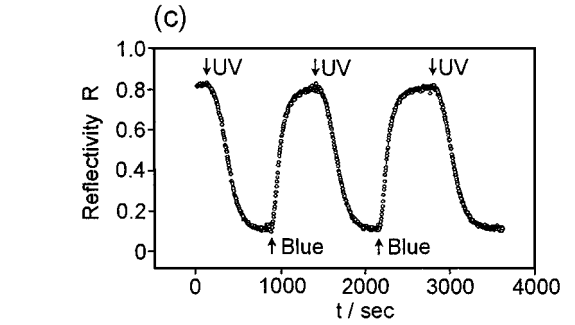

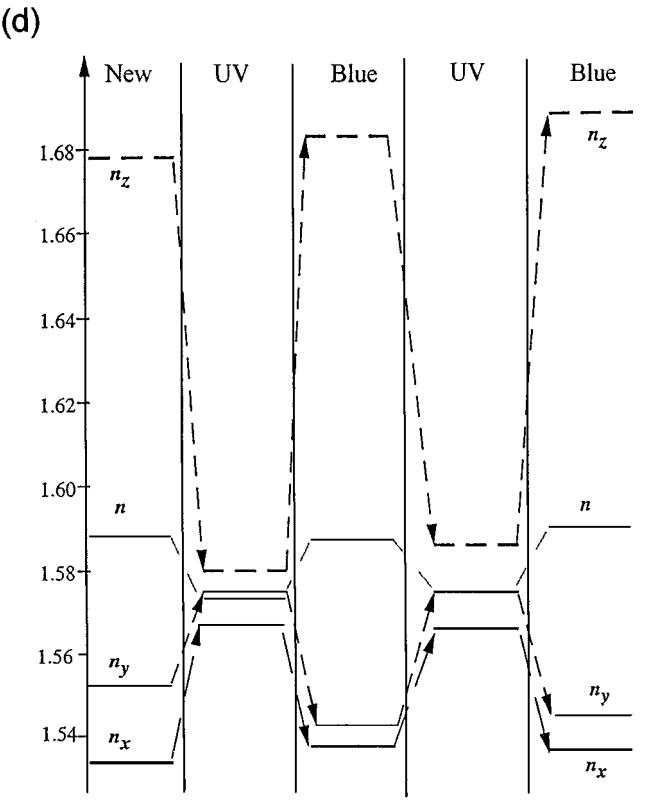

Figure 35 (*Continued*)

as given in Figure 35(*d*). The mean refractive index, $(n_x + n_y + n_z)/3$, is also depicted in this figure. In all the columns, a small and persistent in-plane anisotropy $(n_y - n_x)$ can be noted between the dipping direction (y) and the direction (x) perpendicular to it. This is due to the LBK film deposition process where the flow field orients the rods parallel to the transfer direction.

Figure 35(*d*) also shows in the columns labeled *New* and *Blue*, that the out-of-plane refractive index is much higher than the in-plane refractive indices ($n_z - n_{x,y} \approx 0.14$, where $n_{x,y}$ is the in-plane average refractive index), which means that the side-chains with the azobenzene are highly oriented and point out perpendicularly to the plane of the substrate. In the *New* film this orientation is due to the structure of the monolayer at the air/water interface on the trough, which is conserved by transfer and which is common to all azo-polyglutamates. When the LBK film is exposed to the UV light, n_z decreases significantly ($\Delta n_z \approx 0.1$), and n_x and n_y both increase to nearly the same value [see UV columns in Figure 35(*d*)]. This shows that the polarizability of the azobenzene molecules decreases as a consequence of the change in their electronic and structural properties induced by the photoisomerization from a planar to a bend structure—a change, however, that is fully reversible.

The last examples that we discuss concern the modification of the refractive index of a material by applying a static electric field. The observed optical response can have contributions from various physical phenomena, the most prominent being the Pockels response. This is a $\chi(2)$-process, i.e. due to the second coefficient in a series-development of the optical polarizability of a material with respect to the electromagnetic field (67):

$$|\vec{P}| = \varepsilon_0\left(\chi^0 + \chi^{(1)}|\vec{E}| + \chi^{(2)}|\vec{E}|^2 + \cdots\right). \qquad 38.$$

In all cases of an EO-active material, the symmetry of the response requires a noncentrosymmetric orientation of the NLO-active chromophore. If the sample is prepared by the LBK method, this can be achieved if the $\chi(2)$-active layers are separated from each other by one layer of an inert material, thus creating an ABAB-multilayer stack, with the chromophore layer A being deposited alternating with the buffer material B.

The molecule used in these studies—an asymmetrically derivatized amphiphilic stilbene analogue (compound 15)—is shown in Figure 36(*a*). Sample preparation was performed by organizing the dye molecules as a monomolecular layer at the water/air interface and then depositing onto an Ag-coated substrate two of these monolayers on the upstroke separated by an inert polyglutamate monolayer deposited at the downstroke. This way, the noncentrosymmetric architecture of the NLO-active chromophore layers needed for electrooptical measurements was ensured. The angular scan of this sample shows the excitation of a surface plasmon mode as given in Figure 36(*b*), *full squares*.

(a)

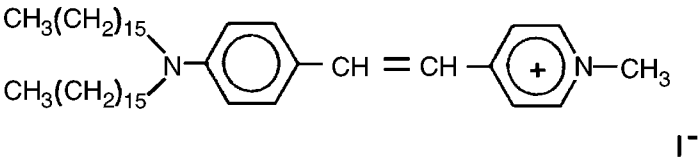

15

(b)

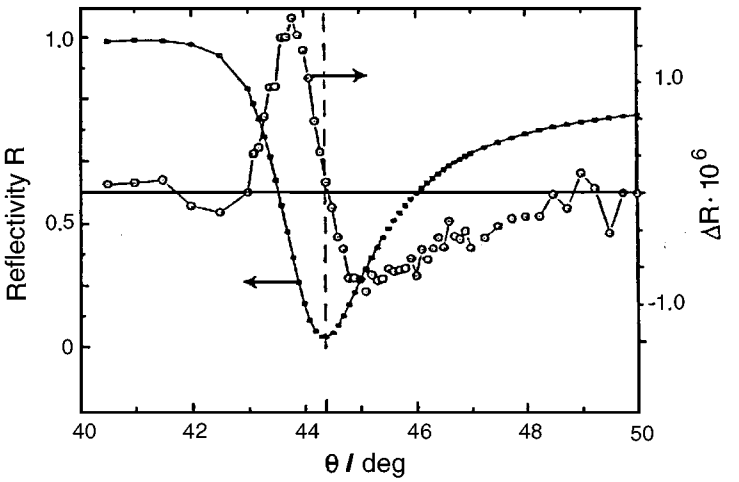

Figure 36 (*a*) Structural formula of the amphiphilic NLO-active stilbene derivative (compound 15). (*b*) *R*-vs-θ, (-■-), and ΔR-vs.-θ scan, (-O-) for a double layer of the stilbene chromophore (compound 15).

A top electrode was required in order to apply an electric DC field across this ultrathin film sample, in addition to the bottom electrode (the latter carrying the surface plasmon mode). Since direct evaporation of a metal layer onto this thin LBK assembly was not possible without shortcuts, another strategy was taken. The top electrode was prepared by evaporation onto a separate glass slide, which was then mechanically pressed against the NLO-active film using a 3-μm-thick mylar film as a spacer. Because the changes of the refractive index induced by an applied electric DC field were too small to be measured directly, a lock-in technique had to be used. To this aim, the applied voltage was modulated at $f = 2.23$ kHz with an amplitude of $U = 30$ V (peak to peak). This generated a slight intensity modulation of the reflected light which could be monitored with

a phase- and frequency-sensitive detector locked to 2.23 kHz. The amplitude of this modulation is a measure of the electric field-induced refractive index change in the thin film, and hence is proportional to the electro-optical coefficients. The obtained data are plotted in Figure 36(*b*). They indicated that by this technique relative reflectivity changes of better than $\Delta R/R = 10^{-6}$ can be detected. The quantitative evaluation of the electro-optical coefficients is not exactly possible, mostly because the electric field strength cannot be determined sufficiently accurately. A rough estimate, however, gave a Pockels response of this material of $\chi^{(2)}_{333} = 1.6$ pm/V (10).

As in all examples given in this review, a much more detailed and precise evaluation of thickness and refractive index data of thin films was possible if their thickness allowed for the excitation of waveguide modes that could be evaluated. This also holds true for the quantitative determination of anisotropic indices and the various coefficients of the $\chi(2)$-tensor describing the nonlinear properties of a thin film. Samples prepared by the LBK method can be assembled into thicknesses large enough to allow for an analysis of linear and nonlinear optical data by waveguide spectroscopy. However, if polymer films, functionalized by the addition of NLO chromophores, are prepared by spin-coating, additional processing steps are required to ensure the noncentrosymmetric distribution of the dyes. Typically, this is done by electric field poling, either using a chorona discharge or by means of two electrodes (68).

The latter approach was taken in the example presented in Figure 37. The sample was a thin spin-cast film of PMMA as host material, doped with 8% (weight/weight) Disperse Red 1 (DR1) as guest [structural formula (compound 16) given in Figure 37(*a*)]. The waveguide was sandwiched between two evaporated Ag electrodes and poled for 40 min at $T = 80°$C with $U = 210$ V. In order to demonstrate the sensitivity of the technique, the sample was allowed to relax for 2 weeks, a period during which most of the polar orientation of the chromophores decayed (69).

Figure 37 gives the results of the reflectivity scans for s- and p-polarization obtained for the angular range between $\theta = 15°$ and $\theta = 67°$. The Fresnel fit curves of the *R*-versus-θ scans [full curves in Figures 37(*b*) and (*d*), respectively] describe the experimental data rather well—an indication that the lateral heterogeneities of the sample within the area of the laser spot are rather moderate. These simulations indicate that a description of the film with a thickness of $d = 2.074$ μm and an anisotropic uniaxial dielectric tensor with an ordinary component $\varepsilon'_0 = 2.292$ and an extraordinary component $\varepsilon'_e = 2.302$ is sufficient. The analysis of the electrooptical ΔR-data [Figures 37(*c*) and (*e*)] give the two relevant Pockels coefficients $\chi^{(2)}_{113} = 2.76$ pm/V and $\chi^{(2)}_{333} = 6.74$ pm/V.

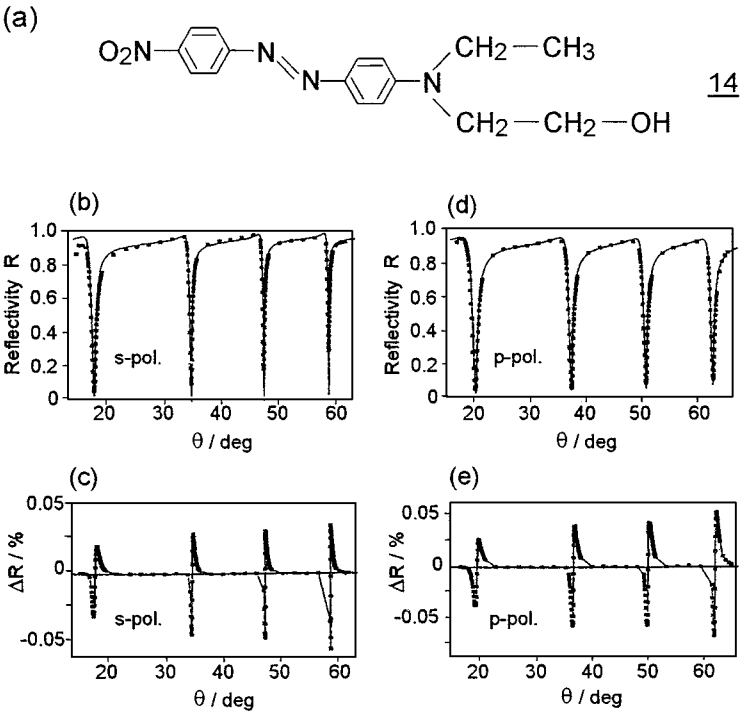

Figure 37 (*a*) Structural formula of DR1, compound 16, mixed into the PMMA waveguide layer. (*b*) and (*d*), reflectivity R-vs-θ, respectively; (*c*) and (*e*), ΔR-vs-θ scans, respectively, as obtained for a PMMA/DR1-sample with s- and p-polarized light (as indicated). *Full curves* in (*b*) and (*d*) are Fresnel fit calculations to the data points. The curves in (*c*) and (*e*) are only guides to the eye.

CONCLUSIONS

Surface plasmon- and waveguide spectroscopies have matured into largely accepted and internationally employed experimental techniques offering a highly sensitive tool for the characterization of structural and optical properties of interfaces and thin films. The fact that this surface light can be used in configurations with different substrate materials—noble metals, oxides (70), polymers—in contact with vacuum, air (or any other gas), as well as liquids, makes it a versatile method, well suited for physicochemical studies of interfacial properties and processes. We have limited the discussion here to the use of these bound modes in a reflection mode, where the information about the interface or the thin film deposited was derived from the observation of the laser light

elastically reflected. However, the concept of evanescent wave optics also refers to the whole range of phenomena and formats of optical experiments known from plane waves— "normal" photons—interacting with matter: Besides elastic processes, this includes scattering (71); refraction; diffraction (72); interference (73) or microscopy (11, 74) observed with bound waves; the wide scenario of inelastic processes, e.g. Brillouin- (75) and Raman-spectroscopies (76, 77); and fluorescence schemes (18, 78). Here, the methodological development is progressing and the obtainable information on details of interfacial architectures still growing. Another promising direction is combining evanescent wave optics with near-field concepts in an effort to overcome the spatial resolution limits of far-field recording, but also aiming at introducing novel contrast mechanisms for the differentiation between different materials at the nanoscopic level (79). The field is still rapidly moving!

ACKNOWLEDGMENTS

This review summarizes the work of many friends and colleagues, and it is my pleasure to acknowledge their contribution. This holds, in particular, for the PhD dissertations of E Aust, H Bock, M Büchel, U Fernandez-Horn, W Hickel, G Kleideiter, T Liebermann, A Nemetz, D Piscevic, M Veith, T Vogt, and M Weisser. Y Geerts synthesized the azosilane compound; the polyaniline and sulfonated polyaniline were from G Advincula, the ionenes came from W Meyer, and the azo-functionalized polyglutamates were prepared by H Menzel. The functionalized thiols were obtained from Boehringer Mannheim, Werk Tutzing. G Jung and his team at the University of Tübingen provided the functionalized phenol derivatives. B Menges in our group was the expert for the grating preparation; the integrated Mach-Zehnder interferometer was designed and fabricated at the Institut für Mikrotechnik, Mainz (IMM). Figure 2 was printed by D Johannsmann, Figure 5 by T Liebermann, and Figure 14(*a*) by Naoko Mitsuzawa. Last but not least I'd like to mention the many intellectual contributions by a number of colleagues. In particular I profited from discussions with G Advincula, A Badia, CW Frank, S Mittler-Neher, O Prucker, and Z Sekkat, who worked with me at the MPI for Polymer Research in Mainz and/or at the Department of Chemical Engineering, Stanford University. Financial support came from the Deutsche Forschungsgemeinschaft (DFG); the Bundesministerium für Bildung, Wissenschaft, Forschung und Technologie (BMBF); Boehringer Mannheim; and the National Science Foundation (NSF) through the Center on Polymer Interfaces and Macromolecular Assemblies (CPIMA).

Literature Cited

1. Saleh BEA, Teich MC. 1991. *Fundamentals of Photonics*. New York: Wiley
2. Axelrod D, Burghardt TP, Thompson NL. 1984. *Annu. Rev. Biophys. Bioeng.* 13:247–68
3. Moses T, Shen YR. 1991. *Phys. Rev. Lett.* 67:2033–37
4. Habicht J. 1998. PhD thesis. Johannes Gutenberg-Universität, Mainz, Germany
5. Burstein E, Chen WP, Chen YJ, Hartstein A. 1972. *J. Vac. Sci. Technol.* 11:1004–19
6. Raether H. 1988. *Springer Tracts in Modern Physics*, Vol. 111. Berlin: Springer-Verlag
7. Ushioda S, Sasaki Y. 1983. *Phys. Rev. B* 27:1401–4
8. Aust E, Ito S, Sawodny M, Knoll W. 1994. *Trends Polym. Sci.* 2:313–23
9. Swalen JD. 1979. *J. Phys. Chem.* 83:1438–45
10. Knoll W. 1997. *Handbook of Optical Properties—Optics of Small Particles, Interfaces, and Surfaces*, ed. RE Hummel, P. Wißmann, 2:373–400. Boca Raton, FL: CRC
11. Aust E, Ito S, Knoll W. 1994. *Scanning* 16:353–61
12. Otto A. 1968. *Z. Phys.* 216:398–409
13. Hickel W, Rothenhäusler B, Knoll W. 1989. *J. Appl. Phys.* 66:4832–36
14. Kretschmann E, Raether H. 1968. *Z. Naturforsch. Teil A* 23:2135–36
15. Knobloch H, Brunner H, Leitner A, Aussenegg F, Knoll W. 1993. *J. Chem. Phys.* 98:10093–95
16. Knoll W. 1991. *Makromol. Chem.* 192: 2827–56
17. Attridge JW, Daniels PB, Deacon JK, Robinson GA, Davidson GP. 1991. *Biosens. Bioelectron.* 6:201–24
18. Knoll W, Zizlsperger M, Liebermann T, Arnold S, Badia A, et al. 1998. Submitted for publication
19. Gordon JG II, Swalen JD. 1977. *Opt. Commun.* 22:374–78
20. Peterlinz KA, Georgiadis RM, Herne TM, Tarlov M. 1997. *J. Am. Chem. Soc.* 119: 3401–2
21. Bunjes N, Schmidt EK, Jonczyk A, Beyer D, Ringsdorf H, et al. 1997. *Langmuir* 13: 6188–94
22. Lee DL. 1986. *Electromagnetic Priniciples of Integrated Optics*. New York: Wiley
23. Chang K, ed. 1991. *Handbook of Microwave and Optical Components*. New York: Wiley
24. Stegeman GI, Stolen RH. 1989. *J. Opt. Soc. Am. B* 6:652–728
25. Hunsperger RG. 1984. *Integrated Optics: Theory and Technology*. Berlin: Springer-Verlag
26. Goos F, Hänchen H. 1947. *Ann. Phys.* 1:333–68
27. Tien PK. 1977. *Rev. Mod. Phys.* 49:361–407
28. Hickel W, Knoll W. 1990. *Appl. Phys. Lett.* 57:1286–88
29. Ulman A. 1991. *Ultrathin Organic Films*. San Diego: Academic
30. Kuhn H, Möbius D, Bücher H. 1972. *Physical Methods of Chemistry*, ed. A Weissberger, BW Rossiter, pp. 577–692. New York: Wiley
31. Knoll W. 1996. *Curr. Opin. Colloid Interface Sci.* 1:137–43
32. Kienle S, Lingler S, Kraas W, Offenhäusser A, Knoll W, et al. 1997. *Biosens. Bioelectron.* 12:779–86
33. Roberts G. 1990. *Langmuir-Blodgett Films*. New York: Plenum
34. Petty MC. 1996. *Langmuir-Blodgett Films*. Cambridge, UK: Cambridge Univ. Press
35. Gaines GL. 1966. *Insoluble Monolayers at Liquid-Gas Interfaces*. New York: Wiley-Intersci.
36. Hickel W, Duda G, Jurich M, Kröhl T, Rochford K, et al. 1990. *Langmuir* 6:1403–7
37. Schmidt A, Mathauer K, Reiter G, Foster MD, Stamm M, et al. 1994. *Langmuir* 10:3820–26
38. Sagiv J. 1980. *J. Am. Chem. Soc.* 102:92–95
39. Sekkat Z, Wood J, Geerts Y, Knoll W. 1996. *Langmuir* 12:2976–80
40. Decher G, Hong JD. 1991. *Ber. Bunsenges. Phys. Chem.* 95:1430–34
41. Advincula R, Aust E, Meyer W, Knoll W. 1996. *Langmuir* 12:3536–40
42. Sekkat Z, Knoll W. 1997. *Adv. Photochem.* 22:117–95
43. Lawall R, Knoll W. 1994. *J. Appl. Phys.* 76:5764–68
44. Tamada K, Hara M, Sasabe H, Knoll W. 1997. *Langmuir* 13:1558–66
45. Leckband DE, Schmitt FJ, Israelachvili JN, Knoll W. 1994. *Biochemistry* 33:4611–24
46. Advincula G, Frank CW, Roitman D, Sheats J, Moon R, et al. 1998. *Mol. Cryst. Liq. Cryst.* In press
47. Spinke J, Liley M, Schmitt FJ, Guder HJ, Angermaier L, et al. 1993. *J. Chem. Phys.* 99:7012–19
48. Spinke J, Liley M, Guder HJ, Angermaier L, Knoll W. 1993. *Langmuir* 9:1821–25
49. Knoll W, Liley M, Piscevic D, Spinke J,

Tarlov MJ. 1997. *Adv. Biophys.* 34:231–50
50. Hara M, Sasabe H, Knoll W. 1996. *Thin Solid Films* 273:66–69
51. Veith M. 1995. PhD thesis. Johannes Gutenberg-Universität, Mainz, Germany
52. Fischer B, Fischer TM, Knoll W. 1994. *J. Appl. Phys.* 75:1577–81
53. Veith M, Worm J, Fischer TM, Mittler-Neher S, Knoll W. 1998. *Sens. Actu. B.* Submitted for publication
54. Helm CA, Knoll W, Israelachvili J. 1991. *Proc. Natl. Acad. Sci. USA* 88:8169–73
55. Widrig CA, Chung C, Porter MD. 1991. *J. Electroanal. Chem.* 310:335–59
56. Zhong CJ, Porter MC. 1997. *J. Electroanal. Chem.* 425:147–52
57. Yang DF, Wilde CP, Morin M. 1997. *Langmuir* 13:243–47
58. Fernandez U, Fischer TM, Knoll W. 1993. *Opt. Commun.* 102:49–52
59. Veith M, Müller K, Mittler-Neher S, Knoll W. 1995. *Appl. Phys. B* 60:1–4
60. Lukosz C, Tiefenthaler K. 1988. *Sens. Actu. B* 15:273–91
61. Brosinger F, Freimuth H, Lacher M, Ehrfeld W, Gedig E, et al. *Sens. Actu. B* 44:350–55
62. Weisser M, Tovar G, Mittler-Neher S, Knoll W, Brosinger F, et al. 1998. *J. Appl. Phys.* Submitted for publication
63. Zizlsperger M, Knoll W. 1998. *Progr. Colloid Polym. Sci.* In press
64. Gibson RE, Loeffler OH. 1941. *J. Am. Chem. Soc.* 63:898–906
65. Kleideiter G, Lechner MD, Knoll W. 1998. *Macroevol. Chem. Phys.*
66. Büchel M, Sekkat Z, Paul S, Weichart B, Menzel H, et al. 1995. *Langmuir* 11:4460–66
67. Shen YR. 1984. *The Principles of Nonlinear Optics*. New York: Wiley
68. Knoll W. 1993. *Mat. Sci. Technol.* 12:529–96.
69. Weiss S, Aust EF, Meyer W, Knoll W. 1996. *J. Non-linear Opt. Phys. Mater.* 5:269–84
70. Miller CE, Meyer WH, Knoll W, Wegner G. 1992. *Ber. Bunsenges. Phys. Chem.* 96:869–79
71. Rothenhäusler B, Knoll W. 1987. *Opt. Commun.* 63:301–4
72. Rothenhäusler B, Knoll W. 1987. *Appl. Phys. Lett.* 51:783–85
73. Rothenhäusler B, Knoll W. 1988. *Appl. Phys. Lett.* 52:1554–56
74. Rothenhäusler B, Knoll W. 1988. *Nature* 332:615–17
75. Lee S, Hillebrands B, Dutcher J, Stegeman GI, Knoll W, et al. 1990. *Phys. Rev. B* 41:5382–87
76. Knoll W, Philpott MR, Swalen JD, Girlando A. 1982. *J. Chem. Phys.* 77:2254–60
77. Nemetz A, Knoll W. 1996. *J. Raman Spectrosc.* 27:587–92
78. Knoll W, Philpott MR, Swalen JD, Girlando A. 1981. *J. Chem. Phys.* 75:4795–99
79. Rücker M, Knoll W, Rabe JP. 1992. *J. Appl. Phys.* 72:5027–31